Photocatalytic mineralization and degradation kinetics of sulphamethoxazole and reactive red 194 over silver-zirconium co-doped titanium dioxide: Reaction mechanisms and phytotoxicity assessment

Graphical Abstract

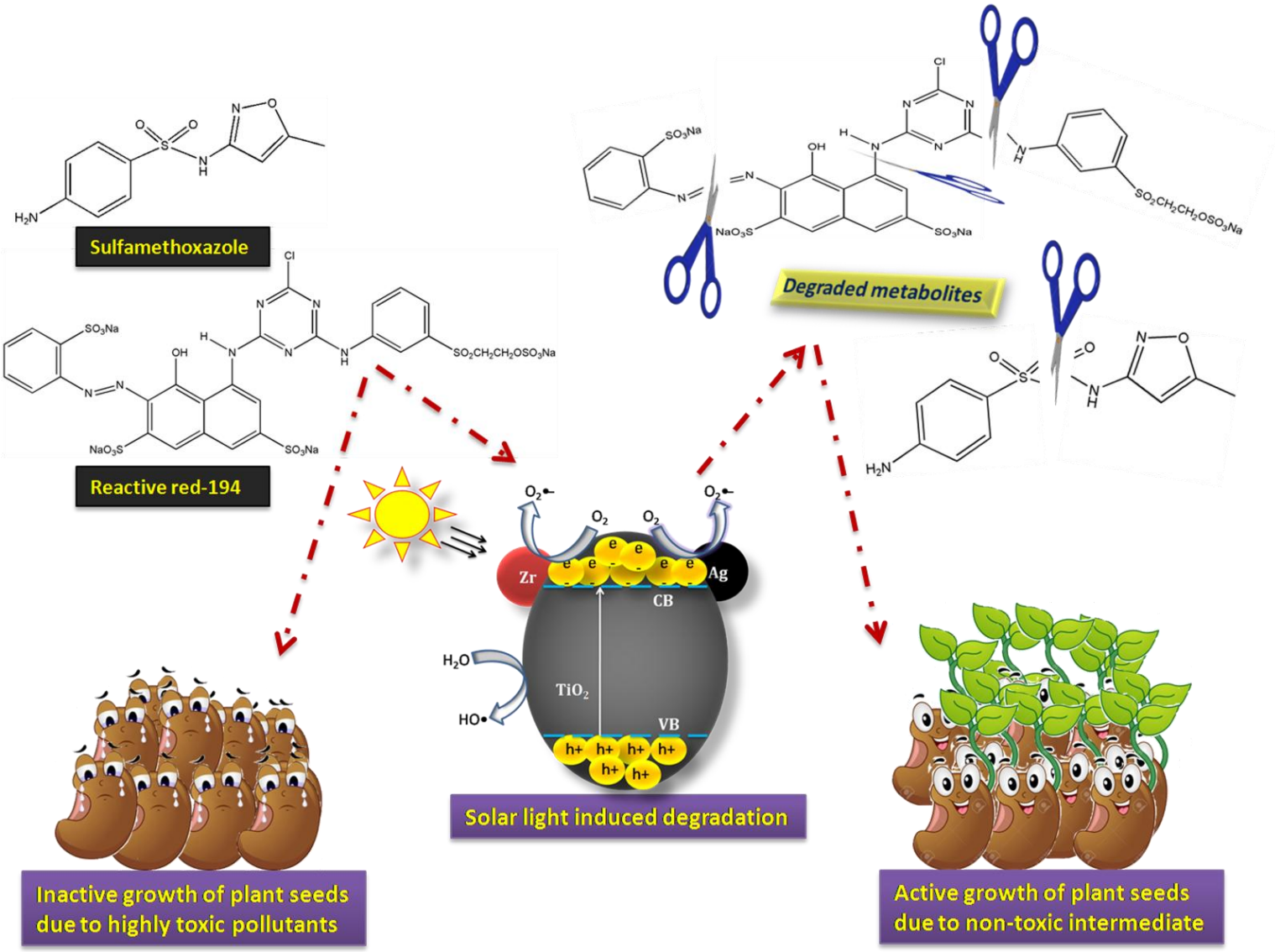

Highlights

- Zr and Ag modified TiO_2 composite was used for degradation of SMX and RR-194
- Mineralization pathway and phytotoxicity of degraded metabolites was evaluated
- Phytotoxicity tests revealed low-toxic intermediates were generated in degradation
- •OH and $•O_2-$ radicals are found to be the main ROS on the photocatalyst surface

Photocatalytic mineralization and degradation kinetics of sulphamethoxazole and reactive red 194 over silver-zirconium co-doped titanium dioxide: Reaction mechanisms and phytotoxicity assessment

Saraschandra Naraginti [a], Yi Li [a]*, Gianluca Li Puma [c]*

[a] Key Laboratory of Integrated Regulation and Resource Development on Shallow Lakes, Ministry of Education, College of Environment, Hohai University, Nanjing – 210098, PR China

[c] Environmental Nanocatalysis & Photoreaction Engineering, Department of Chemical Engineering, Loughborough University, Loughborough LE11 3TU, United Kingdom

Corresponding authors

_____

Email: envly@hhu.edu.cn (Yi LI)

Email: g.lipuma@lboro.ac.uk (Gianluca LI PUMA)

Abstract

The photodegradation and phytotoxicity of the pharmaceutical antibiotic, sulphamethoxazole (SMX) and the azo-dye reactive-red-194 (RR194) under visible-light irradiation of TiO_2 nanoparticles modified by silver and zirconium was investigated. The results indicated that sulphamethoxazole and its toxic degradation by product, 3-amino-5-methylisoxazole and RR-194 could be degraded efficiently by the co-doped Zr/Ag-TiO_2 catalyst. PL studies and ROS generation results suggested that the effective charge separation was carried out while irradiation of the modified TiO_2 nanoparticles. Phytotoxicity tests demonstrated lower percentage of germination in *P. vulgaris* (40%), *V. radiata* (30%) and *P. lunatus* (30%) of the seeds treated with 50 ppm of SMX, compared to the seeds treated with the degradation products (100%). The results with 50 ppm of RR-194 also showed lower percentage of germination in *P. vulgaris* (40%), *V. radiata* (50%) and *P. lunatus* (30%) compared to the degradation products (100%). Furthermore, significant increase in root and shoot development was observed in the seeds treated with the degraded products when compared with SMX and RR-194. Overall, this study contributes to further understanding the photodegradation mechanisms, degradation products and environmental fate of SMX and RR-194 in water which helps in the evaluation and mitigation of the environmental risk of SMX and RR-194 for water reuse and crop irrigation.

Keywords: Photocatalyst; Dyes; Antibiotics; Wastewater; Phytotoxicity

1. Introduction

The extensive utilization of antibiotics in aquaculture, stockbreeding and human medicine have raised significant environmental concerns due to the observed increase in antibiotics resistant bacteria and genes [1-2]. In 2013, China consumed approximately 92,700 tons of antibiotics, 53,800 tons of which have been released into the environment [3]. Often these antibiotics have been detected in lakes, rivers, wastewater effluents [4], estuarine and coastal waters [5, 6]. According to USEPA many antibiotics are reported as chemical contaminants of emerging concern, without much regulation and the effect on human health and the environment is inadequately understood [7].

Sulphonamides are belongs to a category of synthetic antibiotics prepared from sulphanilic acid which function as bacteriostatics by suppressing dihydrofolic acid generation. They have prolonged persistence in the environment due to their low degree of biodegradability. The concentration levels of these sulphonamides in water has been reported in the range of 0.13–1.9 μgL^{-1} [8], and could accumulate in several organisms such as bacteria [9,10]. Sulphamethoxazole belongs to a broad spectrum sulphonamide, and is one of the most extensively prescribed antibiotics worldwide. After administration, the metabolism of the content takes place in the liver, however the unmetabolized [11] and active metabolites [12,13] are then excreted in urine or feces ultimately reaching the gray water sewer systems and/or conventional wastewater treatment plants [14]. SMX is a refractory pollutant and not easily biodegraded by conventional treatments those employed in sewage treatment plants [15]. This necessitates the utilization of high efficiency materials and tertiary oxidative treatment for the effective degradation of SMX. In addition, the degradation products of SMX, such as 3-amino-5-methylisoxazole, could cause a harmful threat to wildlife [16]. Studies have reported the

formation of 3-amino-5-methylisoxazole during chemical [17-19] and microbial [20,21] degradation of SMX, and fewer studies have reported its further transformation.

Other common classes of contaminants often found in water and wastewater are dyes used in paints manufacturing and textiles. The azo dye RR-194 is a very common in cotton dyeing. Azo dyes are highly carcinogenic, harmful to human health and cause reduced light penetration in aqueous environments adversely affecting photosynthesis [22]. Conventional methods including coagulation, activated-carbon adsorption, biodegradation and membrane filtration have been used for wastewater decolorization. However, these methods cannot completely remove the contaminants and their degradation products and often need further waste disposal after treatment [23]. Thus, the treatment of dyes demands the development of new and effective processes for their removal. Altogether, the untreated release of antibiotics, EDCs and dye effluents would not only induce serious health and environmental hazards but also has a strong impact on the fertility of soil.

Heterogeneous photocatalysis with visible light irradiation of modified titanium dioxide (TiO_2) nanoparticles has emerged one of the effective treatment methods for dyes and pharmaceuticals removal [24-27] and for water reuse in agriculture. Co-doping of TiO_2 with two different atoms has attracted significant interest since the dual effect can synergistically affect the photocatalytic activity of semiconductor materials compared to doping with a single element [28, 29]. Addition of Ag and Zr can reduce the recombination of electrons and holes by efficient trapping of electrons. Further, Zr is an isoelectric element exhibiting deep energy level doping properties [30].

In this study Ag and Zr modified TiO_2 nanoparticles have been utilized in the degradation of SMX and RR-194. The possible degradation mechanisms were investigated by HPLC and LC-

ESI/MS analysis. Water reuse necessitates the assessment of the phytotoxicity of the SMX, RR-194 and their corresponding degradation products. Therefore the phytotoxicity of the degradation products and parent pollutants was investigated upon three plant seeds *P. vulgaris, V. radiata* and *P. lunatus* to determine the environmental impact of the treated water.

2. Materials and methods

2.1 Materials

Titanium (IV) isopropoxide, terepthalic-acid (TA), nitroblue-tetrazolium-chloride (NBT) and sulphamethoxazole (SMX) from Sigma, reactive red-194 from a local textile industry, hydrazine hydrate, zirconyl nitrate [$ZrO(NO_3)_2$], isopropanol, potassium iodide (KI), EDTA, potassium dichromate ($K_2Cr_2O_7$), ascorbic acid, ethanol and tween-20 are purchased from Alibaba Chemicals.

2.2 Synthesis and characterization of metal modified TiO_2 nanoparticles

Metal modified TiO_2 nanoparticles (Ag/TiO_2 and $Zr/Ag\text{-}TiO_2$) were prepared according to the methodology reported in our previous work [31]. BRUKER D8-Advance X-ray diffractometer was used to obtain XRD data with Cu Kα source (λ=1.5406 A^o). Imaging of the nanoparticles was carried out using a high resolution transmission electron microscope (JEOL JEM 2100). UV-Vis spectra (DRS mode) were recorded on a JASCO V–670 UV–Vis spectrophotometer. The photoluminescence (PL) spectra were obtained on a HITACHI F-7000 fluorescence spectrophotometer. XPS data was acquired on a Kratos Axis Ultra 165 Spectrometer equipped with a monochromated Al Kα X-ray source (hα = 1486.6 eV). A micrometrics ASAP 2020 V4.03 analyzer was used to obtain BET surface area and pores size distributions of the synthesized nanoparticles. The zeta potentials of TiO_2, Ag/TiO_2 and $Zr/Ag\text{-}$

TiO_2 nanoparticles were measured at 25 °C by dynamic laser light scattering using Malvern Zetasizer Nano ZS90.

2.3 Degradation experiments and determination of by products

A laboratory scale photoreactor (Fig. 1), was designed and utilized for all photocatalytic degradation experiments, which consists of a visible light source (Osram 150 W tungsten halogen lamp with 100 mW/cm^2 intensity, λ: 400–800 nm) positioned at the center of the reactor. Six reaction tubes, 50 ml each, 10 mm internal diameter, were placed at a distance of 15 cm from the light source. Dry air was purged continuously into all the reaction tubes through small pipes at a flowrate of 2 L min^{-1}, to keep the aqueous solution saturated with oxygen and the catalyst particles in suspension. The inner surface of the photoreactor hood was fitted with a highly polished reflector in order to ensure the maximum reflection and utilization of the light source. The bottom of the reactor was equipped with an electric fan to cool the cabinet during the experiments maintaining a constant temperature (25±2 °C).

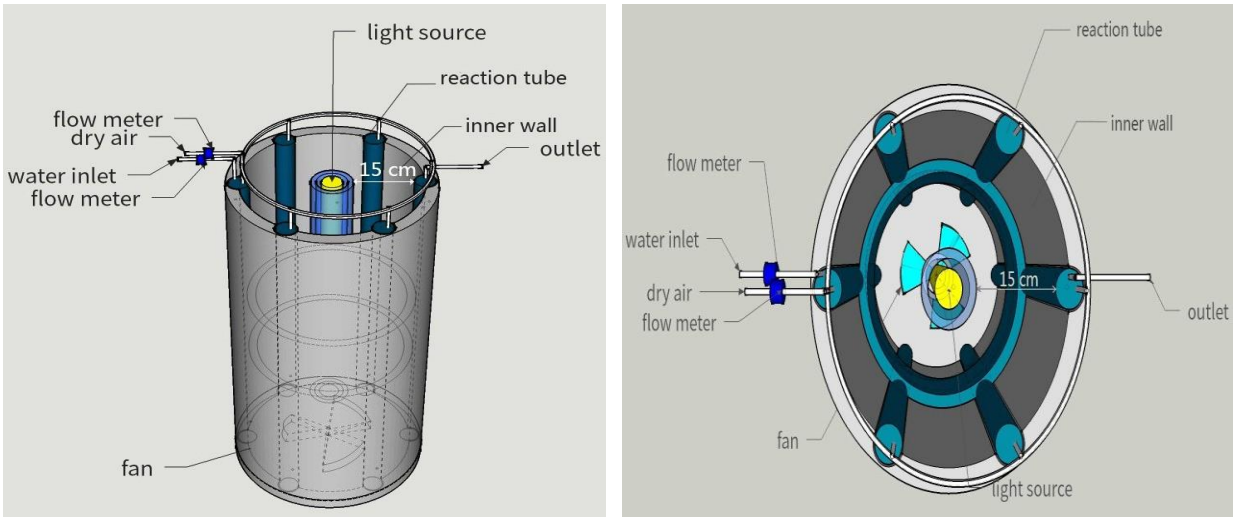

Fig.1. (a) Multitube reactor set-up for the degradation experiments; (b) top view of the reactor

The remnant concentration of SMX was determined by a HPLC (Agilent 1260 series) equipped with an Eclipse XDBC18 (4.6 x 150 mm, 5 µm) reverse phase column. Initially 100 mL of SMX solution (20 ppm) and 50 mg of the catalyst were stirred in the dark for 60 min to obtain absorption–desorption equilibrium, [32,33]. The UV detector wavelength was 203 nm, while the mobile phase consisted of water and acetonitrile (70:30 v/v) fed at a flow rate of 1 mL min^{-1} for 60 minutes [34]. Similar procedure was followed to achieve absorption–desorption equilibrium during degradation of RR-194 (25 ppm), as discussed above. Small sample aliquots (2 mL) were collected at regular time intervals and the solids were separated through centrifugation at 2000 rpm for 5 min. The supernatants were analyzed by a JASCO V–670 UV–Vis spectrophotometer, recording the absorption at 522 nm.

Further, the analysis of SMX and RR-194 degradation products was carried by liquid chromatography tandem mass spectrometer (Agilent 1290 LC system, Agilent 6460 Triple Quadrupole LCMS/MS system with the Zorbax eclipse plus C18 column). Water and acetonitrile (70:30 v/v) as mobile phase at a flow rate of 0.2 mL min^{-1} was used for SMX analysis (60 min of run time), while methanol and water (30:70 v/v) was used for the analysis of RR-194 (60 min of run time). Spray Ionization (ESI) under the flow of helium gas (1 mL min^{-1}) was used to obtain mass spectra at a fragment voltage of 16 V.

2.4 Active species scavenging experiments

To investigate the main reactive oxygen species (ROS), various scavenging experiments were conducted during the photocatalytic degradation processes. These were performed by adding ascorbic acid for O_2•− scavenging [35], EDTA for h^+ scavenging [36], $K_2Cr_2O_7$ for e^- scavenging [37], isopropanol for •OH scavenging [38], and KI for both •OH and h^+ scavenging [35,36] during the photocatalytic reactions. For quantification of •OH, the photocatalyst (50 mg)

was added to a 50 ml mixture of TA (3 mmol) and NaOH (10 mmol) aqueous solution. Thus, TA quickly reacts with generated •OH radicals to form a fluorescent active 2-hydroxyterephthalic acid (TAOH) which emits fluorescence at 426 nm on excitation at 312 nm (Scheme 2). The amount of •OH radicals generated during irradiation should be directly proportional to the photoluminescent intensity of TAOH. Similarly, the quantification of $\bullet O_2-$ radicals was carried out by monitoring NBT (2×10^{-4} M) absorption peak at 259 nm. Upon reaction with $\bullet O_2^-$ radicals NBT can be peculiarly reduces to form an insoluble purple formazan compounds in the aqueous solutions (Scheme 1). The quantification of $\bullet O_2^-$ was done by analyzing the decrease in the NBT concentration using a UV–Vis spectrophotometer.

2.5 Phytotoxicity Assessment

The phytotoxicity assessment test of toxicants and their corresponding metabolites was carried out on three types of crop seeds, *P. vulgaris, V. radiata* and *P. lunatus,* using 50 ppm concentration of SMX, RR-194 and with the irradiated samples containing the reaction degradation products. The degraded metabolites of SMX and RR-194 were extracted by ethyl acetate then dried and dissolved in 10 mL distilled water to obtain a final concentration of 50 ppm. The phytotoxicity test was carried out by following the prescribed guidelines in the literature [39,40] with few modifications. Seeds of each crop type (10 no) were sterilized using 1-5 % sodium hypochlorite solution (15 min) followed by thorough washing with distilled water. They were then immersed for 60 min in the SMX, RR-194 aqueous solutions and in the samples subjected to photocatalytic degradation using 100 mL Erlenmeyer flasks containing the contaminants and their respective degradation products. Seeds immersed in distilled water were used as controls for comparison. The seeds were then placed on a wet cotton in different petri

dishes and incubated at 25 ± 1^{o}C in dark (24 h). The germinated seeds were selected for further toxicity studies.

Further phytotoxicity assays were continued in beakers containing 1.5 % agar media (30 mL) and 50 ppm of SMX, RR-194 and the reaction degradation products. The agar containing beakers were instantly hardened in a freezer. Germinated seeds from the petri plates were placed on the surface of the agar in each beaker and then placed in incubator at 25 ± 1^{o}C in dark. Control experiments were included with seedlings on agar alone without the contaminants. After 5 days of incubation the plants were slowly removed from the agar media and lengths of the root and shoots were measured. The experiments were carried out in triplicate and the average data was shown in the present study.

3. Results and discussion

3.1 Characterization

Fig. S1a shows the UV–Vis absorption spectra of synthesized bare TiO_2, Ag/TiO_2 and Zr/Ag-TiO_2 respectively. Red shifts were observed as a result of the incorporation of silver and zirconium into TiO_2 matrix in both Ag/TiO_2 (absorption edge shift from 340 to 380) and Zr/Ag-TiO_2 (maximum red shift from 380 nm to 400 nm). The red shifted spectra show a possible evidence for good interaction between TiO_2, Ag and Zr species. Hence, the observed red shift behavior clearly justifies the change in the light absorption characteristics. The energy band gap values (Fig.S1b) of bare TiO_2, Ag/TiO_2 and Zr/Ag-TiO_2 were calculated to be around 3.18 eV, 3.08 eV and 2.87 eV, respectively. These results suggest that the Zr/Ag-TiO_2 nanoparticles could possibly show a higher photocatalytic activity in the visible region.

The X-ray diffraction pattern of TiO_2, Ag/TiO_2 and $Zr/Ag\text{-}TiO_2$ nanoparticles (Fig. 2) displayed diffraction peaks corresponding to the TiO_2 anatase (JCPDS 21-1272) crystalline phase. Because of their low concentration levels (0.2-0.8 mole %), peaks related to metallic Zr or Ag were not observed in the XRD pattern, which suggested that dopants did not alter the crystallinity of TiO_2. Furthermore, the representing oxide compounds (Zr_xO_y or Ag_xO_y) were not found either, suggesting that nano Zr and Ag particles were well diffused into the TiO_2 crystal lattice, thus enhancing the visible light absorption.

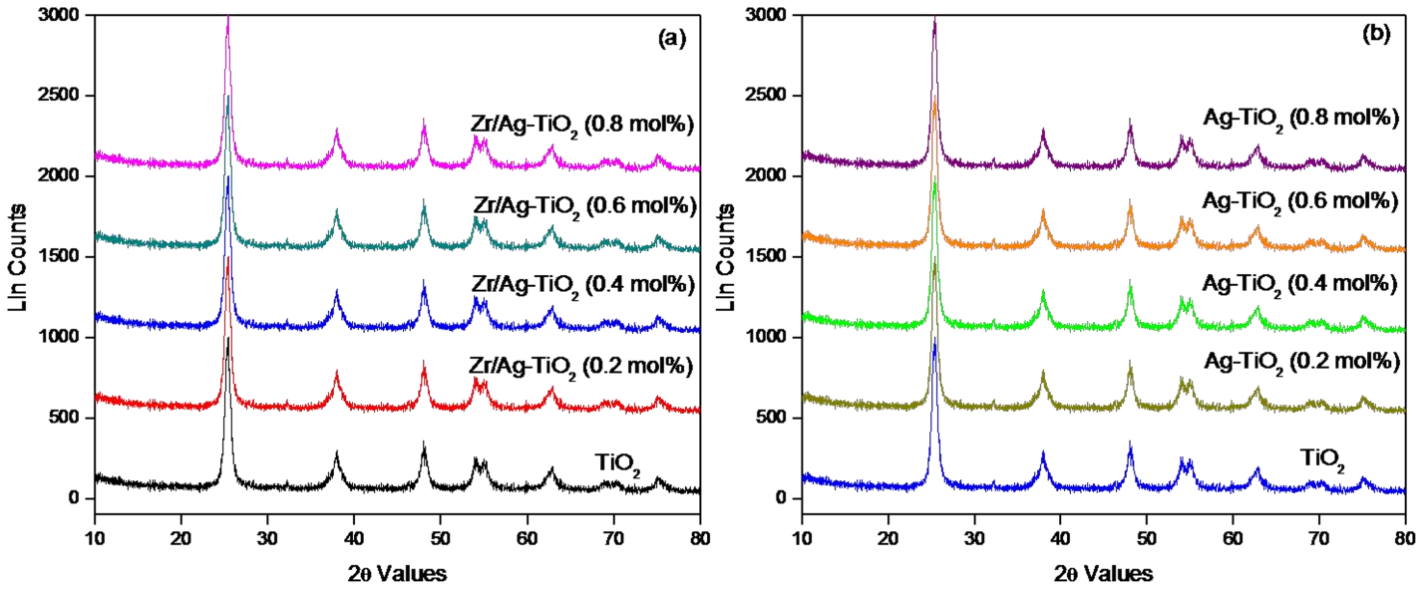

Fig. 2 X-ray diffraction pattern of the synthesized nanoparticles

TEM images of Ag/TiO_2 and $Zr/Ag\text{-}TiO_2$ (Fig. S2a and S3a) suggested uniform distribution of the particles ranging from 10-17 nm and 7-15 nm respectively. High resolution TEM pictures were (Fig. S2b and S3b) employed to observe the microstructure of the photocatalysts, for analyzing the particle grains and their boundaries. The SAED patterns of the prepared nanoparticles (Fig. S2c and S3c) clearly showed dark fringes corresponding to the standard diffraction rings of the polycrystalline anatase phase as indexed. Diffraction fringes

signals related to other phases were not found. The EDAX profile (Fig. S2d and S3d) evidenced the elemental composition of the prepared samples.

The variations in zeta potentials of synthesized nanoparticles in their aqueous solutions are shown in Fig. S3. From the results it was found that the pHzpc of TiO_2, Ag-TiO_2 and Zr/Ag-TiO_2 is 6.38, 6.13 and 6.09 respectively. At lower pH levels the photocatalyst surface becomes more positive at pH below pHzpc and more negative above it [41,42]. With increase in negative zeta potential values, the stability of the catalyst increases at higher pH levels. From the results it reveals that Zr/Ag-TiO_2 particles shown relatively better stability at higher pH. The relative zeta-potential values were from 18.8 to 27.9 mV at pH 9, while it was altered between 5.8 to 15.1 mV at pH 3. It indicates that, at lower pH levels the metal modified TiO_2 nanoparticles defended destabilization, and the zeta-potential values of did not increase majorly at pH < pHzpc than over pHzpc [43].

The evident XPS spectra for Ag 3d, Zr 3d, Ti 2p and O 1s levels were carried out to analyze whether the doped metals interwove into TiO_2 crystal lattice or formed surface compounds. The relevant high-resolution XPS spectrum of Ag at 3d core levels shown in Fig. 3a indicates that the binding energies for Ag $3d_{5/2}$ and Ag $3d_{3/2}$ are observed at 368.1 and 374.1 eV which matches with the bulk metallic silver [44,45]. The binding energies for Zr $3d_{5/2}$ and Zr $3d_{3/2}$ observed at 182.4 and 184.6 eV (Fig. 3b), are attributed to the +4 oxidation state of zirconium [46]. XPS spectrum of Ti 2p (Fig. 3c) shown peaks at 459.2 and 464.9 eV were belongs to Ti $2p_{3/2}$ and Ti $2p_{1/2}$ core levels respectively [47,48]. These results designate that titanium represent +4 oxidation state. Fig. 3d shows the broad spectrum of Zr/Ag-TiO_2 nanocomposite, indicates that in Zr/Ag-TiO_2 Ag, Ti and Zr metal ions were present in their highest oxidation state.

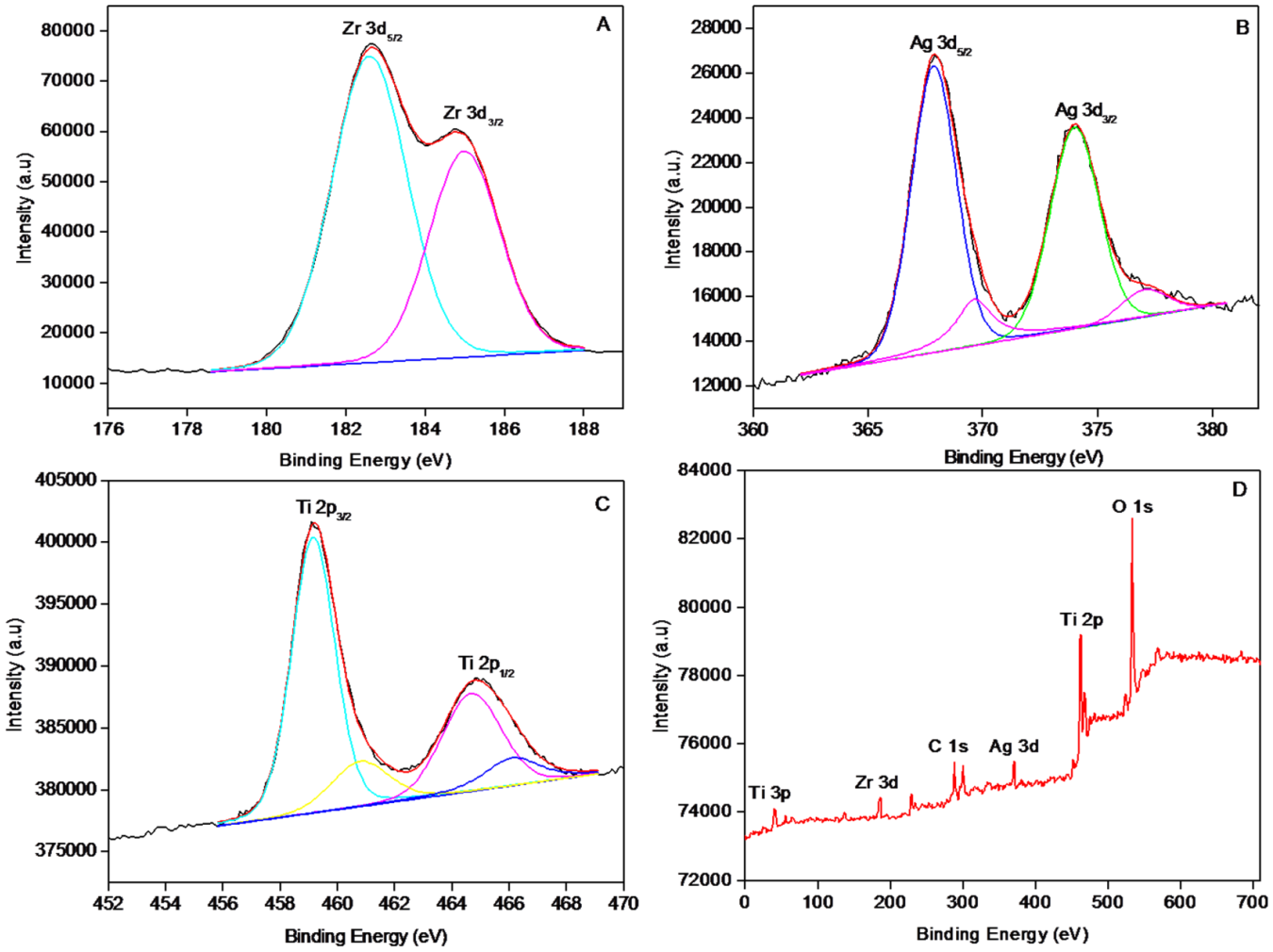

Fig. 3 High resolution XPS spectrum of (a) Ag at 3d, (b) Zr at 3d, (c) Ti at 2p core levels and (d) broad spectrum of Zr/Ag-TiO2 nanocomposite

The production of $\bullet O_2^-$ radical during the photocatalytic process was determined by the NBT transformation method [49] (Scheme 1). Fig. S8 b showed the kinetic NBT transformation percentage at different time intervals during irradiation. The higher generation rates of $\bullet O_2^-$ (Fig. S7b) with increase in irradiation time could be ascribed to the lower energy band gap of Zr/Ag-TiO_2 and lower rate of photogenerated electron–hole recombination as shown by the PL spectra. The generated photo electrons remaining in the conduction band (CB) during the photoexcitation

of the semiconductor photocatalyst, reacted with adsorbed O_2 molecules to generate highly reactive $\bullet O_2^-$. Since the energy band gap of Zr/Ag-TiO_2 was the smallest, the photogenerated electrons from the valence band (VB) could be easily transferred to the CB with more effective charge separation and reduced electron-hole pair recombination. This eventually led to higher decomposition of SMX and RR-194, which was further supported by the active scavenging experiment results (Fig. S7).

Quantification of •OH radicals during photocatalytic process was carried out by using terephthalic-acid photoluminescence probe method (TA-PL). Terephthalic-acid readily reacts with the produced •OH radicals and forms a highly fluorescent 2-hydroxyterephthalic acid (TAOH) [50-52] (Scheme 2). The rate of formation of TAOH with pure TiO_2 was negligible consistent with its large band gap. In contrast, the formation of TAOH was significant with Zr/Ag-TiO_2 nanoparticles showing the higher rate, as expected consistent with its smaller band gap (Fig. S8a). The above results indicated that $\bullet O_2^-$ and •OH radicals played a major role in the degradation of both SMX and RR-194 under visible light.

3.2 Degradation kinetics and pathway of SMX and RR-194

Langmuir–Hinshelwood model (Eq.1) was used to describe the photodegradation kinetics of SMX and RR-194 under visible light (Eq.1), which illustrates that the reactions take place at a solid-liquid interface.

$$\ln [C_o/C_t] = k_r K_t = K_{apr} t \text{ ---------- (1)}$$

The degradation of both SMX (Fig. 4 a) and RR-194 (Fig. 4 b) with visible-light irradiation revealed pseudo first-order kinetics with regression coefficients (R^2) ≥ 0.88. Among the various tested photocatalysts, Zr/Ag-TiO_2 nanocomposite exhibited the best activity with rate constants of k = 0.131 min^{-1} and k = 0.183 min^{-1} for SMX and RR-194 respectively. It is evident

to indicate that Zr/Ag-TiO_2 nanocomposite had more than 1.5 times better degradation efficiency in degrading SMX compared to the other visible light photocatalyst (e.g., Cu-TiO_2 nanoparticles [53]).

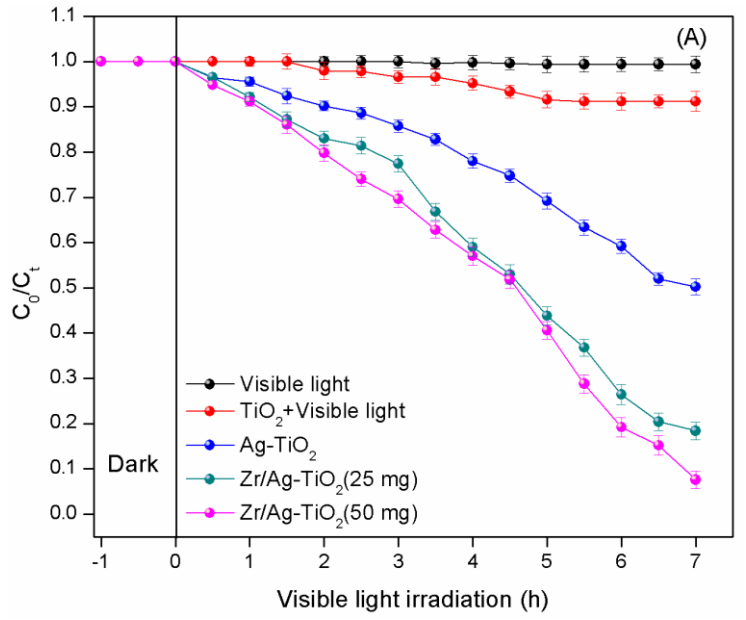

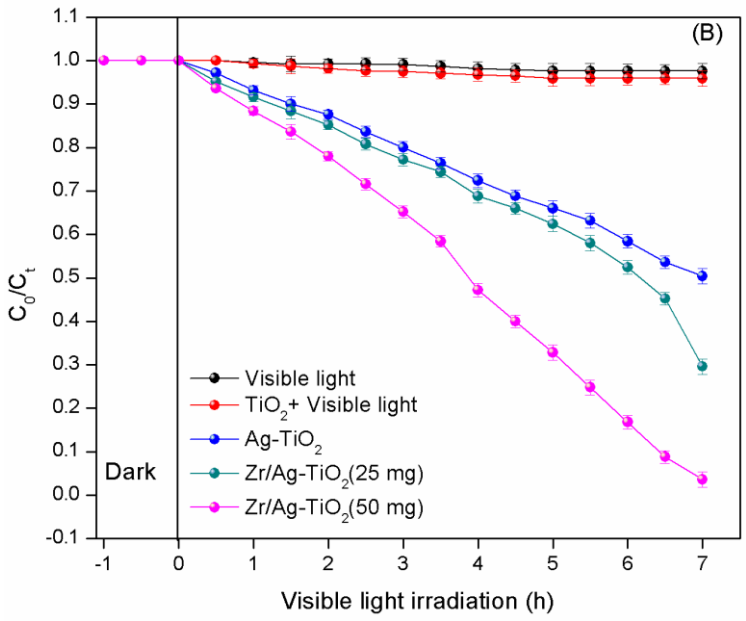

Fig. 4 Kinetic curves of SMX (a) and RR-194 (b) degradation suing different photocatalysts under visible light

LC–ESI/MS analysis of the sampled before and after irradiation was performed to elucidate the reaction mechanisms of photocatalytic degradation of SMX and RR-194 over visible light irradiated Zr/Ag-TiO_2 nanoparticles. LC-MS analysis of the SMX degraded samples evidenced the presence of compounds with molecular weights 252.2 (M+3), 238.2 (M+2), 226.2 (M-2), 186.2 (M-3) and 184.2 (M-1) which could be interpreted as structures A, B, C, D and G (Fig. 5 & S5). The byproduct L was identified as 3-amino-5-methylisoxazole (3A5MI) with m/z = 99.9 for $[M-1]^+$ which results from the cleavage of the δ-position and further oxidation by •OH. The byproduct F was identified as sulfanilamide ($C_6H_8N_2O_2S$) as a result of γ-cleavage, the important intermediate during SMX degradation. The degraded product of SMX also showed m/z values of 213 (M+1), 199.9 (M+1), 106.9 (M+1), 145.9 (M-4), 160.9 (M-4), 174.9 (M-3) and 117.9 (M-2) which represents the structures E, F, K, J, I, H and M (Fig. 5 & S5). The fragment ion corresponds to m/z 157.1 suggests that the SMX degradation initiates by attacking the •OH radicals on the isoxazole ring. Nonselective attack by •OH on SMX molecule at various sites is the first oxidation step of SMX, this results in the establishment of hydroxylated derivatives, which are further oxidized by •OH to form additional byproducts. The structures J and L were identified as maleic acid and cyclohexa-2,5-diene-1,4-dione, which could finally lead to formation of H_2O and CO_2 [54].

The LC-MS/MS pattern of the RR-194 degraded sample also showed the presence of different compounds with m/z values of 753.2 (M+1), 679.2 (M+3), 632.6 (M-4), 527 (M+3), 511.1 (M+3) and 453.1 (M-2) which could be interpreted structures A, B, C, D, E and F (Fig. 6 & S6). The RR-194 degraded sample also showed peaks with m/z values of 385.8 (M-), 340.1 (M+4), 327.7(M+2), 309.7 (M-3), 287.7 (M-3), 223.8 (M-3), 193.8 (M+2), 178.8 (M+2), 129.9

(M+4) and 117.9 (M+3) which represents the structures G, H, I, J, K, L, M, N, O and P (Fig. 6 & S6).

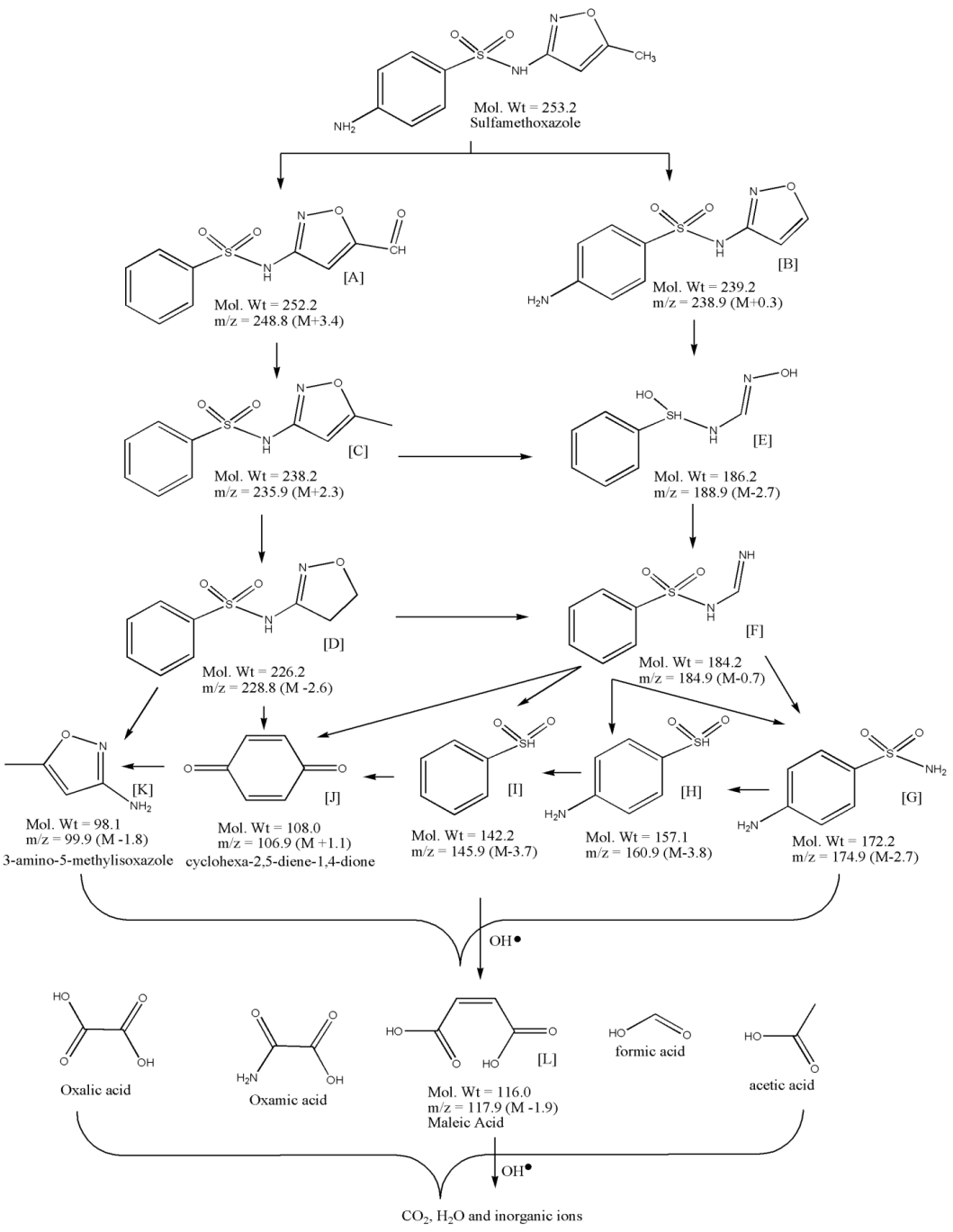

Fig. 5 Transformation pathway of SMX by Zr/Ag-463 TiO2 (50 mg) nanocomposite under visible light

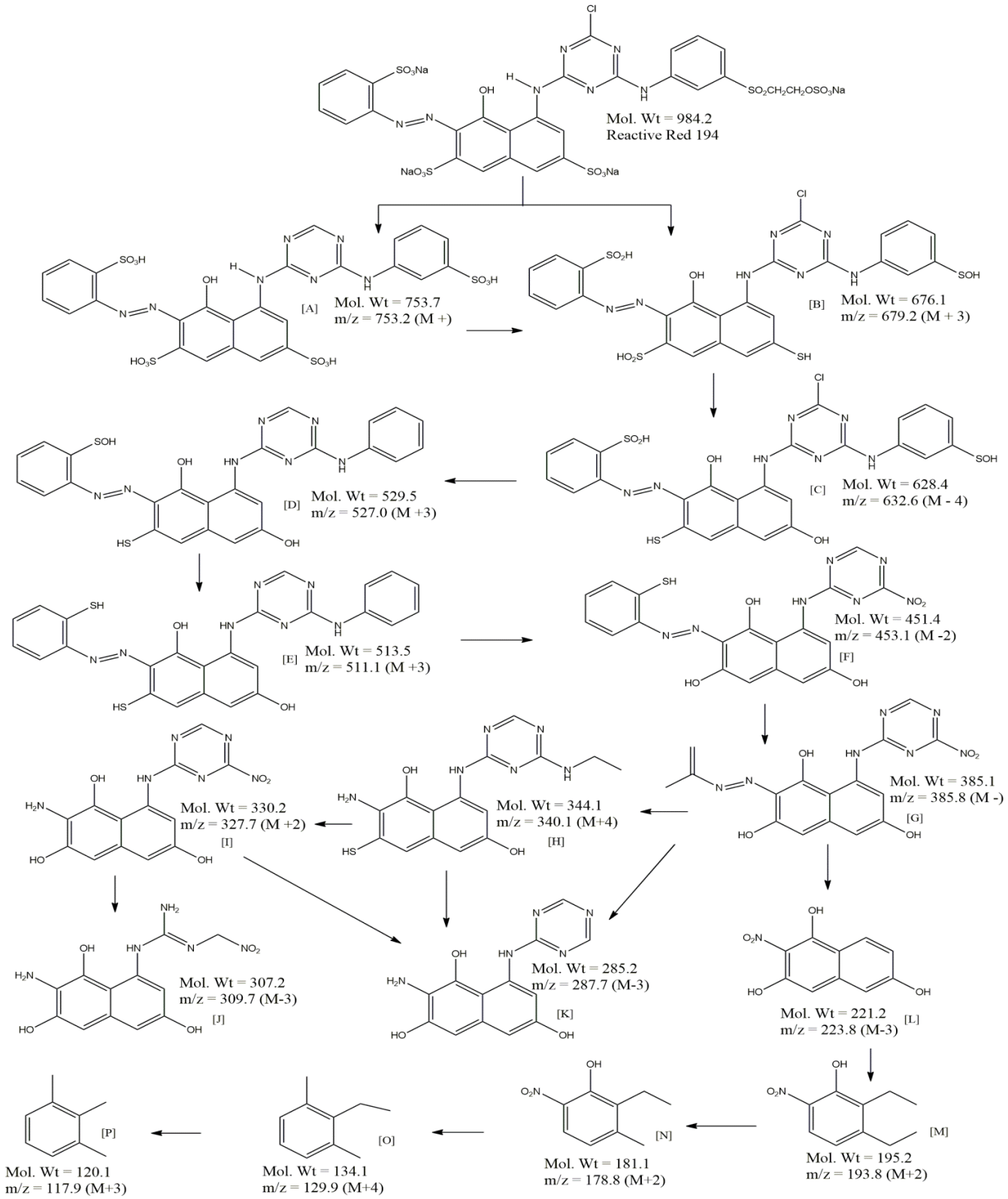

Fig. 6 Transformation pathway of RR-194 by Zr/Ag-TiO2 (50 mg) nanocomposite under visible light

3.3 Active species scavenging experiment

Different scavenging experiments were carried out in order to investigate the main radical species involved in the photocatalytic degradation of SMX and RR-194 under visible light irradiation. Ascorbic acid, EDTA, $K_2Cr_2O_7$ and isopropylalcohol were used as $\bullet O_2^-$, h^+, e^- , and •OH scavengers, while potassium iodide (KI) was used as scavenger for both •OH and h^+ (Fig. S7 a & b). By adding scavengers to the reaction solution the decreased photocatalytic activity was in the following order: isopropanol > ascorbic acid > EDTA > potassium iodide > potassium dichromate > no scavenger. In the N_2 saturated solution, SMX and RR-194 degradation over Zr/Ag-TiO_2 was significantly inhibited. Thus, these findings proposed that the degradation of SMX and RR-194 was most interfered by adding isopropyl alcohol and ascorbic acids to the reaction solution, confirms that the •OH and $\bullet O_2^-$ radicals were the main reactive oxygen species (ROS) during the photodegradation processes. Moreover, the addition of EDTA and $K_2Cr_2O_7$ demonstrated minimal decrease in the photoctalytic degradation process compared to isopropyl alcohol and ascorbic acid, which incriminate that the •OH and $\bullet O_2^-$ were the primary ROS responsible for the effective degradation of the contaminants.

3.4 Phytotoxicity

SMX (50 ppm) highly inhibited the germination of *P. vulgaris, V. radiata* and *P. lunatus,* reducing it to 40 %, 30 % and 30 % respectively. Less germination was also found in all three seeds *P. vulgaris* (40 %), *V. radiata* (50 %) and *P. lunatus* (30 %) treated with RR-194. However, the seeds treated in 50 ppm of the photodegradion products and distilled water (control) exhibited 100% germination (Table 1). Furthermore, the toxicity of pure SMX solutions is also reflected on the plant root and shoots length, leading only to minimum growth of shoots in *P. vulgaris* (5.30 ± 0.31 cm), *V. radiata* (0.80 ± 0.61 cm) and *P. lunatus* (0.90 ± 0.87 cm).

Similarly, pure RR-194 solution significantly restricted the growth of shoots in *P. vulgaris* (4.92 ± 0.15 cm), *V. radiata* (1.12 ± 0.98 cm) and *P. lunatus* (1.02 ± 0.19 cm). On the contrary higher shoot and root lengths were observed in the case of seeds grown in degraded products, as well as, in the control (Table 1) (Fig. 7). Collectively, these phytotoxicity results indicated the ability of the prepared nanoparticles to degrade the toxic contaminants SMX and RR-194 and to reduce the toxicity of the treated water.

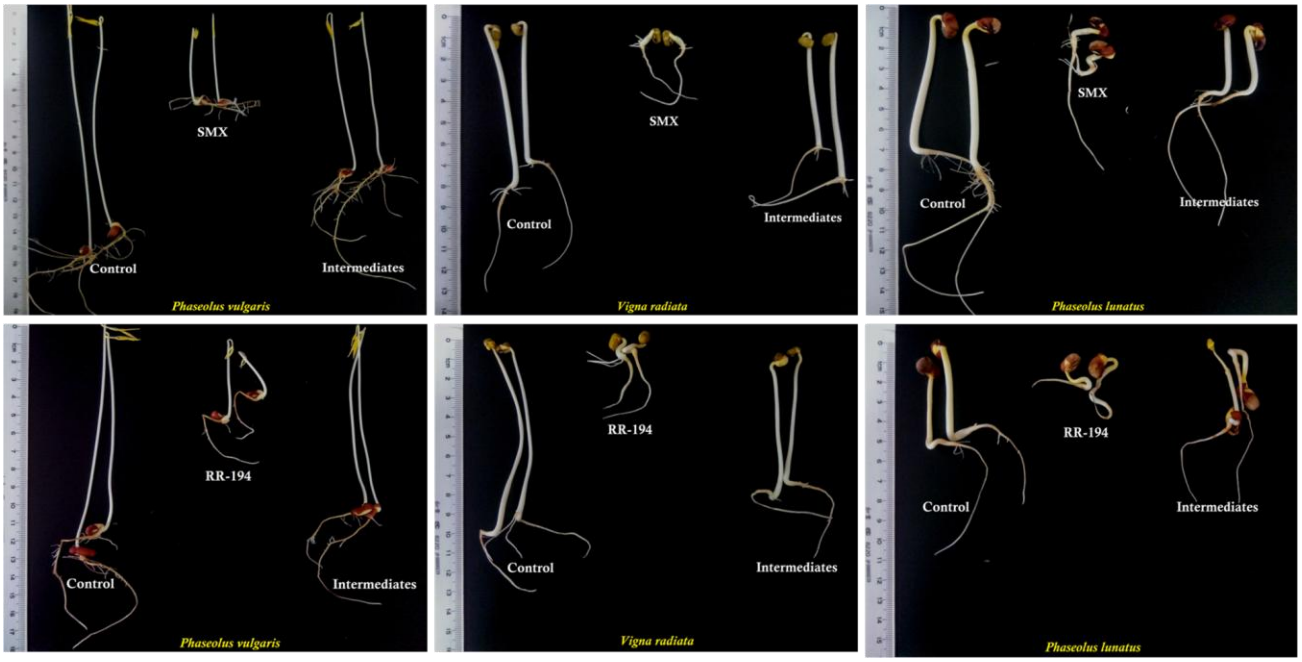

Fig. 7 Phytotoxicity assessment of SMX, RR-194 and their metabolites after 5 days

3.5 Photocatalytic mechanism

It is well evidenced that 'Ag' traps the electrons from CB of TiO_2, while doping with 'Zr' reduces the recombination of electrons and holes by further electron trapping [55]. The VB electrons of Zr/Ag-TiO_2 could easily migrate to the CB by absorbing visible light, leaving holes in the VB Eq (2). These photogenerated electrons are scavenged by the oxygen molecules absorbed on the surface of the photocatalyst, producing highly reactive superoxide anion radicals ($\bullet O_2^-$), which are according to the scavenging experiments play a key role in the

photodegradation of the contaminants (Eq. 3). Likewise, the photogenerated holes in the VB of TiO_2 readily oxidize H_2O and OH^- into hydroxyl (•OH) radicals (Eq. 4 and 5), which significantly promote the photodegradation of SMX and RR-194. Thus, hydroxyl (•OH) and superoxide ($•O_2-$), radicals are the ROS species on the photocatalyst surface that drive the formation of the degradation products (Eq. 6).

$$Zr/Ag\text{-}TiO_2 + h\nu \longrightarrow Zr/Ag\text{-}TiO_2\ (eCB^- + hVB^+) \text{ -------- (2)}$$

$$Zr/Ag\text{-}TiO_2\ (eCB^-) + O_2 \longrightarrow Zr/Ag\text{-}TiO_2 + •O_2 \text{ -------- (3)}$$

$$Zr/Ag\text{-}TiO_2\ (hVB^+) + H_2O \longrightarrow Zr/Ag\text{-}TiO_2 + •OH + H^+ \text{ -------- (4)}$$

$$Zr/Ag\text{-}TiO_2\ (hVB^+) + OH^- \longrightarrow Zr/Ag\text{-}TiO_2 + •OH \text{ -------- (5)}$$

$$SMX \text{ or } RR\text{-}194 + •O_2- + •OH \longrightarrow \text{Degradation product -------- (6)}$$

4. **Conclusions**

Novel TiO_2 nanoparticles modified with silver and zirconium were synthesized and utilized in the photocatalytic degradation of toxic organic pollutants, sulphamethoxazole and reactive red-194 under visible light irradiation. The doping of silver and zirconium improved the photocatalytic activity of TiO_2 under visible light illumination, which resulted from the decrease of the band gap energy. The plausible transformation pathway and degradation products were determined by LC/ESI-MS analysis and the reaction mechanisms were elucidated with radical scavenging experiments. According to phytotoxicity assessment it is suggested that the degraded products induces better growth in root and shoots compare to pure SMX and RR-194 in all three crop seeds (*P. vulgaris*, *V. radiata* and *P. lunatus*), which evidenced that less toxic intermediates were generated during degradation process. Thus, we conceive that the present study provides manifest of Zr/Ag-TiO_2 multifunctional nanomaterials to simultaneously degrade and detoxify

the contaminated water during photocatalysis under visible light irradiation and to provide a potential and effective method for water reuse and for crop irrigation.

Acknowledgements

The study was financially supported by the National Natural Science Foundation of China for Foreign Youth Scholars (Grant No. 51650110501), the China Postdoctoral Science Foundation (Grant No. 2016M591767), the Foundation for Innovative Research Groups of the National Natural Science Foundation of China (Grant No. 51421006), Program for Environmental Protection in Jiangsu Province (Grant No. 2015037), and Priority Academic Program Development of Jiangsu Higher Education Institutions. The Fundamental Research Funds for the Central Universities (Grant No. 2016B10614), Priority Academic Program Development of Jiangsu Higher Education Institutions, and Top-notch Academic Programs project of Jiangsu Higher Education Institutions (TAPP)

References

[1] B. Chen, Y. Yang, X. Liang, K. Yu, T. Zhang, X. Li, Metagenomic profiles of antibiotics resistance genes (ARGs) between human impacted estuary and deep ocean sediments, Environ. Sci. Technol. 47 (2013a) 12753-12760.

[2] Y. Luo, D. Mao, M. Rysz, Q. Zhou, H. Zhang, L. Xu, P.J.J. Alvarez, Trends in antibiotics resistance genes occurrence in the Haihe River, China, Environ. Sci. Technol. 44 (2010) 7220-7225.

[3] Q.Q. Zhang, G.G. Ying, C.G. Pan, Y.S. Liu, J.L. Zhao, Comprehensive evaluation of antibiotics emission and fate in the river basins of China: source analysis, multimedia modeling, and linkage to bacterial resistance, Environ. Sci. Technol. 49 (2015) 6772-6782.

[4] L. Rizzo, C. Manaia, C. Merlin, T. Schwartz, C. Dagot, M.C. Ploy, I. Michael, D. Fatta-Kassinos, Urban wastewater treatment plants as hotspots for antibiotic resistant bacteria and genes spread into the environment: a review, Sci. Total Environ. 447 (2013) 345–360.

[5] A. Shimizu, H. Takada, T. Koike, A. Takeshita, M. Saha, Rinawati, N. Nakada, A. Murata, T. Suzuki, S. Suzuki, N.H. Chiem, B.C. Tuyen, P.H. Viet, M.A. Siringan, C. Kwan, M.P. Zakaria, A. Reungsang, Ubiquitous occurrence of sulfonamides in tropical Asian waters, Sci. Total Environ. 452-453 (2013) 108-115.

[6] R. Mohammadi, B. Massoumi, M. Rabani, Photocatalytic Decomposition of Amoxicillin Trihydrate Antibiotic in Aqueous Solutions under UV Irradiation Using Sn/TiO_2 Nanoparticles, Int. J. Photoenergy. 51 (2012) 1-11.

[7] T. Deblonde, C. Cossu-Leguille, P. Hartemann, Emerging pollutants in wastewater: A review of the literature, Int. J. Hyg. Environ. Health. 214 (2011) 442-448.

[8] A.L. Boreen, W.A. Arnold, K. McNeill, Photochemical fate of sulfa drugs in the aquatic environment: sulfa drugs containing five-membered heterocyclic groups, Environ. Sci. Technol. 38 (2004) 3933–3940.

[9] K. Kümmerer, Antibiotics in the aquatic environment-A review-Part I, Chemosphere. 75 (2009) 417-434.

[10] A. Dirany, I. Sirés, N. Oturan, M.A. Oturan, Electrochemical abatement of the antibiotic sulfamethoxazole from water, Chemosphere 81 (2010) 594–602.

[11] S. Pérez, P. Eichhorn, D.S. Aga, Evaluating the biodegradability of sulfamethazine, sulfamethoxazole, sulfathiazole, and trimethoprim at different stages of sewage treatment, Environ. Toxicol. Chem. 24 (2005) 1361–1367.

[12] M. Cleuvers, Aquatic ecotoxicity of pharmaceuticals including the assessment of combination effects, Toxicol. Lett. 142 (2003) 185–194.

[13] M. Cleuvers, Mixture toxicity of the anti-inflammatory drugs diclofenac, ibuprofen, naproxen, and acetylsalicylic acid, Ecotoxicol. Environ. Saf. 59 (2004) 309–315.

[14] A. Wang, Y.Y. Li, A.L. Estrada, Mineralization of antibiotic sulfamethoxazole by photoelectro-Fenton treatment using activated carbon fiber cathode and under UVA irradiation, Appl. Catal. B 102 (2011) 378–386.

[15] R. Wei, F. Ge, S. Huang, M. Chen, R. Wang, Occurrence of veterinary antibiotics in animal wastewater and surface water around farms in Jiangsu Province, China, Chemosphere 82 (2011) 1408-1414.

[16] M. Gonzalez, T. Hashem, L. Jakob, A. Braum, Oxidative degradation of nitrogen-containing organic compounds: vaccum-ultraviolet (VUV) photolysis of aqueous solutions of 3-amino 5-methylisoxazole, Fresenius' J. Anal. Chem. 351 (1995) 92-97.

[17] M.d.M. Gomez-Ramos, M. Mezcua, A. Agüera, A.R. Fern_andez-Alba, S. Gonzalo, A. Rodríguez, R. Rosal, Chemical and toxicological evolution of the antibiotic sulfamethoxazole under ozone treatment in water solution, J. Hazard. Mater. 192 (2011), 18-25.

[18] S. Gao, Z. Zhao, Y. Xu, J. Tian, H. Qi, W. Lin, F. Cui, Oxidation of sulfamethoxazole (SMX) by chlorine, ozone and permanganateda comparative study, J. Hazard. Mater. 274 (2014) 258-269.

[19] A.G. Trovo, R.F. Nogueira, A. Agüera, A.R. Fernandez-Alba, C. Sirtori, S. Malato, Degradation of sulfamethoxazole in water by solar photo-Fenton: Chemical and toxicological evaluation, Water. Res. 43 (2009) 3922-3931.

462 [20] B. Jiang, A. Li, D. Cui, R. Cai, F. Ma, Y. Wang, Biodegradation and metabolic
463 pathway of sulfamethoxazole by *Pseudomonas psychrophila* HA-4, a newly isolated
464 cold-adapted sulfamethoxazole-degrading bacterium, Appl. Microbiol. Biotechnol. 98
465 (2014) 4671-4681.
466 [21] B. Ricken, P.F. Corvini, D. Cichocka, M. Parisi, M. Lenz, D. Wyss, P.M. Martínez-
467 Lavanchy, J.A. Müller, P. Shahgaldian, L.G. Tulli, Ipso-hydroxylation and subsequent
468 fragmentation: a novel microbial strategy to eliminate sulfonamide antibiotics, Appl.
469 Environ. Microbiol. 79 (2013) 5550-5558.
470 [22] G. R. Li, D. L. Qu, W. X. Zhao, Y. X. Tong, Electrochemical deposition of (Mn,
471 Co)-codoped ZnO nanorod arrays without any template, Electrochem. Commun. 9 (2007)
472 1661–1666.
473 [23] Z. Wang, C. Chen, F. Wu, B. Zou, M. Zhao, J. Wang, C. Feng, Photodegradation of
474 rhodamine B under visible light by bimetal codoped TiO_2 nanocrystals, J. Hazard. Mater.
475 164 (2009) 615–620.
476 [24] L. Gnanasekaran, R. Hemamalini, R. Saravanan, K. Ravichandran, F. Gracia, Vinod
477 Kumar Gupt, Intermediate state created by dopant ions (Mn, Co and Zr) into TiO_2
478 nanoparticles for degradation of dyes under visible light, J. Mol. Liq. 223 (2016) 652–
479 659.
480 [25] Zheng-Hui Ren, Hai-Tao Li, Qiang Gao, HaoWang, Bo Han, Kai-Sheng Xia,
481 Cheng-Gang Zhou, Au nanoparticles embedded on urchin-like TiO_2 nanosphere: An
482 efficient catalyst for dyes degradation and 4-nitrophenol reduction, Mater. Des. 121
483 (2017) 167–175.

[26] Yujie He, Nora B. Sutton, Huub H.H. Rijnaarts, Alette A.M. Langenhoff, Degradation of pharmaceuticals in wastewater using immobilized TiO_2 photocatalysis under simulated solar irradiation, Appl. Catal. B 182 (2016) 132–141.

[27] Lu Lin, Huiyao Wang, Pei Xu, Immobilized TiO_2-reduced graphene oxide nanocomposites on optical fibers as high performance photocatalysts for degradation of pharmaceuticals, Chem. Eng. J. 310 (2017) 389–398.

[28] R. Aiswal, N. Patel, A. Dashora, R. Fernandes, M. Yadav, R. Edla, R.S. Varma, D.C. Kothari, BL Ahuja, A. Miotello, Efficient Co-B-codoped TiO_2 photocatalyst for degradation of organic water pollutant under visible light, Appl. Catal. B 183 (2016) 242-253.

[29] Q. Guo, Z. Zhang, X. Ma, K. Jing, M. Shen, N. Yu, J. Tang, D.D. Dionysiou, Preparation of N,F-codoped TiO_2 nanoparticles by three different methods and comparison of visible-light photocatalytic performances Separ. Puri. Techn. 175 (2017) 305-313.

[30] D. Das, H.K. Mishra, K.M. Parida, A.K. Dalai, Preparation, physico-chemical characterization and catalytic activity of sulphated ZrO_2–TiO_2 mixed oxides, J. Mol. Catal. A Chem. 189 (2002) 271–282.

[31] Saraschandra Naraginti, Finian Bernard Stephen, Adhithya Radhakrishnan, A. Sivakumar, Zirconium and silver co-doped TiO_2 nanoparticles as visible light catalyst for reduction of 4-nitrophenol, degradation of methyl orange and methylene blue, Spectrochim. Acta, Part A. 135 (2015) 814–819.

[32] A. Hernández-Gordillo, V. Rodríguez González, Silver nanoparticles loaded on Cu-doped TiO2 for the effective reduction of nitro-aromatic contaminants, Chem. Eng. J. 261 (2015) 53–59.

[33] E. Bilgin Simsek, Solvothermal synthesized boron doped TiO_2 catalysts: Photocatalytic degradation of endocrine disrupting compounds and pharmaceuticals under visible light irradiation, Appl. Catal. B. 200 (2017) 309–322.

[34] L. Wang, Y. Liu, J. M, F. Zhao, Rapid degradation of sulphamethoxazole and the further transformation of 3-amino-5-methylisoxazole in a microbial fuel cell, Water. Res. 88 (2016) 322-328

[35] S. Song, L. Xu, Z. He, H. Ying, J. Chen, X. Xi and B. Yan, Photocatalytic degradation of C.I. Direct Red 23 in aqueous solutions under UV irradiation using $SrTiO_3/CeO_2$ composite as the catalyst, J. Hazard. Mater. 152 (2008) 1301–1308.

[36] Y. Fu, H. Chen, X. Sun and X. Wang, Combination of cobalt ferrite and graphene: High-performance and recyclable visible-light photocatalysis, Appl. Catal. B. 111–112 (2012) 280–287.

[37] L. S. Zhang, K. H. Wong, H. Y. Yip, C. Hu, J. C. Yu, C. Y. Chan and P. K. Wong, Effective photocatalytic disinfection of *E. coli* K-12 using AgBr-Ag-Bi_2WO_6 nanojunction system irradiated by visible light: The role of diffusing hydroxyl radicals, Environ. Sci. Technol. 44 (2010) 1392–1398.

[38] Z. Pan, E. Stemmler, H. J. Cho, W. Fan, L. LeBlanc, H. H. Patterson and A. Amirbahman, Photocatalytic degradation of 17α-ethinylestradiol (EE2) in the presence of TiO_2-doped zeolite, J. Hazard. Mater. 279 (2014) 17–25.

[39] USEPA, Ecological effects test guidelines. Seed germination root elongationtoxicity test. Office of prevention, Pesticides and Toxic substances 850 4200. Washington DC. EPA 712-C-96-163 (1996).

[40] A.S. Arun Prasad, V.S.V. Satyanarayana, K.V. Bhaskar Rao, Biotransformation of Direct Blue 1 by a moderately halophilic bacterium *Marinobacter* sp. strain HBRA and toxicity assessment of degraded metabolites, J. Hazard. Mater. 262 (2013) 674– 684.

[41] M. Saquiba, M.A. Tariq, M. Faisal, M. Muneer, Photocatalytic degradation of two selected dye derivatives in aqueous suspensions of titanium dioxide, Desalination 219 (2008) 301–311.

[42] M.A. Habiba, I.M.I. Ismail, A.J. Mahmood, M.R. Ullah, Photocatalytic decolorization of brilliant golden yellow in TiO_2 and ZnO suspensions, J. Saudi. Chem. Soc. 16 (2012) 423–429.

[43] Amit Kumar Behera, Ch Venkatanarasimha Rao, Raj Kumar Das, Ardhendu Sekhar Giri & Animes Kumar Golder, Fabrication and characterization of Ag-doped titania: impact of dye-sensitization, phenol decomposition kinetics and biodegradability index, Desalination and Water Treatment. 57 (2016) 9488-9497.

[44] E. Sumesh, M.S. Bootharaju, Anshup, T. Pradeep, A practical silver nanoparticle-based adsorbent for the removal of Hg^{2+} from water, J. Hazard. Mater. 189 (2011) 450–457.

[45] Y. Lai, H. Zhang, K. Xie, D. Gong, Y. Tang, L. Sun, C. Lin, Z. Chen, Fabrication of uniform Ag/TiO_2 nanotube array structures with enhanced photoelectrochemical performance, New J. Chem. 34 (2010) 1335–1340.

549 [46] T. sunekawa, K. Asami, S. Ito, M. Yashima and T. Sugimoto, XPS study of the
550 phase transition in pure zirconium oxide nanocrystallites, Appl. Surf. Sci. 252 (2005)
551 1651–1656
552 [47] K. V. Bineesh, S. Y. Kim, B. R. Jermy and D. W. Park, Catalytic performance of
553 vanadia-doped titania-pillared clay for the selective catalytic oxidation of H_2S, J. Ind.
554 Eng. Chem. 15 (2009) 207–211.
555 [48] Y. Kim, J. Lee, H. Jeong, Y. Lee, M. H. Um, K. M. Jeong, M. K. Yeo and M. Kang,
556 Methyl orange removal over Zn-incorporated TiO_2 photo-catalyst, J. Ind. Eng. Chem. 14
557 (2008) 396–400.
558 [49] K. I. Ishibashi, A. Fujishima, T. Watanab and K. Hashimoto, Detection of active
559 oxidative species in TiO2 photocatalysis using the fluorescence technique, Electrochem.
560 Commun. 2 (2000) 207-210.
561 [50] N. Arunkumar, R. Vijayaraghavan, Enhanced Photocatalytic activity of
562 Nanocrystalline N - doped $ZnSb_2O_6$: role of N doping, cation ordering, particle size and
563 crystallinity, RSC Adv. 4 (2014) 65223-65231.
564 [51] S. Naraginti, Y. Li and Y. Wu, A visible light mediated synergistic catalyst for
565 effective inactivation of E. coli and degradation of azo dye Direct Red-22 with
566 mechanism investigation, RSC Adv. 6 (2016) 75724–75735.
567 [52] N. Tian, H. Huang, Y. He, Y. Guo, T. Zhang, Y. Zhang, Mediator-free direct Z-
568 scheme photocatalytic system: $BiVO_4$/g-C_3N_4 organic–inorganic hybrid photocatalyst
569 with highly efficient visible-light-induced photocatalytic activity, Dalton Trans. 7 (2015)
570 4297-4307.

571 [53] L. F. Chiang, R. Doong, Enhanced photocatalytic degradation of sulfamethoxazole
572 by visible-light-sensitive TiO_2 with low Cu addition, Sep. Purif. Technol. 156 (2015)
573 1003–1010.
574 [54] A. G. Gonc¸alves, J.J.M. Órfão, M.F. R. Pereira, Catalytic ozonation of
575 sulphamethoxazole in the presence of carbon materials: Catalytic performance and
576 reaction pathways, J. Hazard. Mater. 239– 240 (2012) 167– 174.
577 [55] S.T. Pantelides, The electronic structure of impurities and other point defects in
578 semiconductors, Rev. Mod. Phys. 50 (1978) 797-858.

Table

Table 1. Phytotoxicity assessment of SMX, RR-194 and their corresponding degraded metabolites (after 5 days)

	Water	SMX	SMX metabolites	RR-194	RR-194 metabolites
Phaseolus vulgaris					
Germination (%)	100	40	100	40	100
Shoot (cm)	13.27±0.57*	5.30±0.31**	10.15±0.51*	4.92±0.15**	9.45±1.21
Root (cm)	7.67±0.63*	1.43±0.15**	5.92±0.24**	2.41±0.34**	5.87±1.01
Vigna radiata					
Germination (%)	100	30	100	50	100
Shoot (cm)	8.47±0.17**	0.80±0.61*	6.65±0.59	1.12±0.98	7.54±1.66
Root (cm)	5.96±0.51*	2.54±0.31**	4.22±0.54	3.11±1.04	4. 71±0.61*
Phaseolus lunatus					
Germination (%)	100	30	100	30	100
Shoot (cm)	7.98±0.57*	0.90±0.87	4.78±1.01	1.02±0.19**	4.75±0.67*
Root (cm)	8.17±0.38**	2.19±1.05	6.62±0.94	1.81±0.74	5.12±0.86

Values are mean of germination seeds treated with SMX, RR-194 and degraded metabolites, significantly different from the seeds germinated with tap water at*$P < 0.05$, ** $P < 0.01$, by one-way analysis of variance (ANOVA).

Figure

Fig. 1

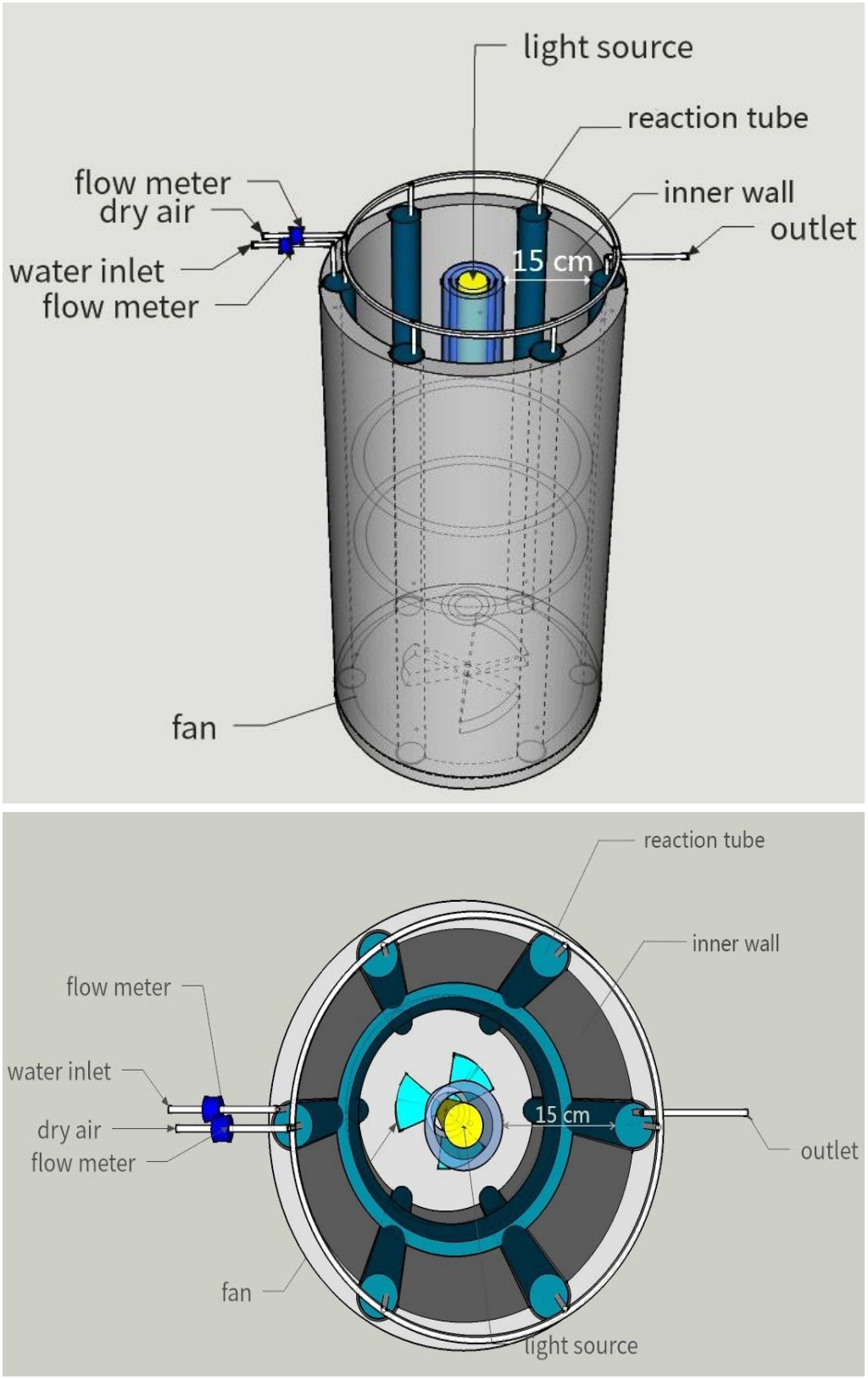
light source
reaction tube
flow meter
dry air
inner wall
outlet
water inlet
flow meter
15 cm
fan
reaction tube
inner wall
flow meter
water inlet
dry air
flow meter
15 cm
outlet
fan
light source

Fig. 2

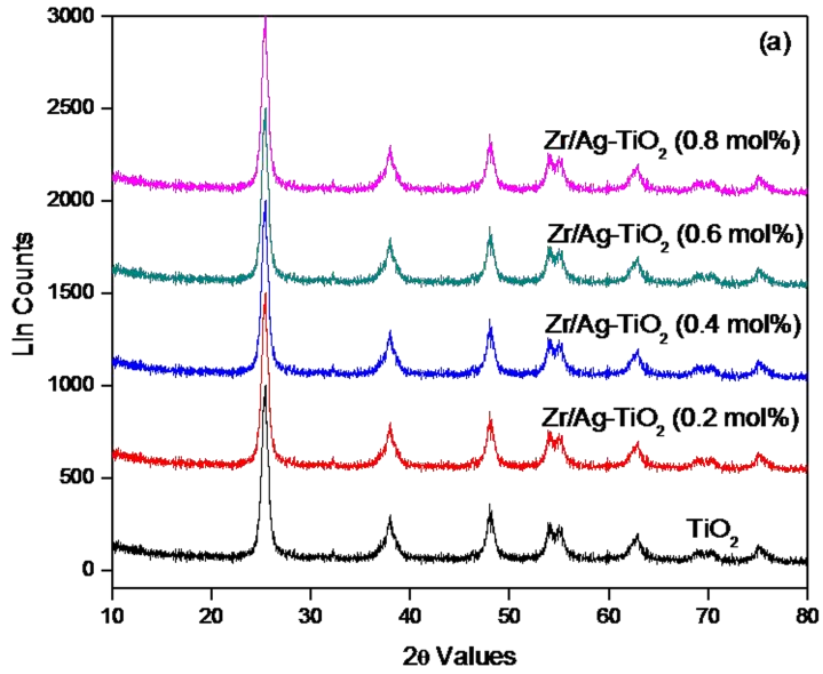
(a)
Zr/Ag-TiO2 (0.8 mol%)
Zr/Ag-TiO2 (0.6 mol%)
Zr/Ag-TiO2 (0.4 mol%)
Zr/Ag-TiO2 (0.2 mol%)
TiO2
Ln Counts
2θ Values
3000
2500
2000
1500
1000
500
0
10
20
30
40
50
60
70
80

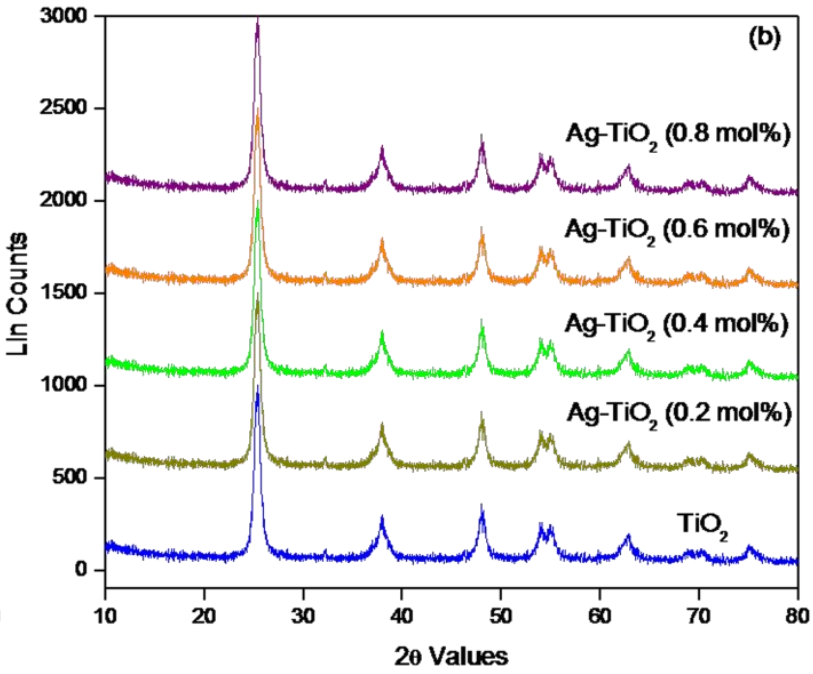
(b)
Ag-TiO2 (0.8 mol%)
Ag-TiO2 (0.6 mol%)
Ag-TiO2 (0.4 mol%)
Ag-TiO2 (0.2 mol%)
TiO2
Ln Counts
2θ Values
3000
2500
2000
1500
1000
500
0
10
20
30
40
50
60
70
80

Fig. 3

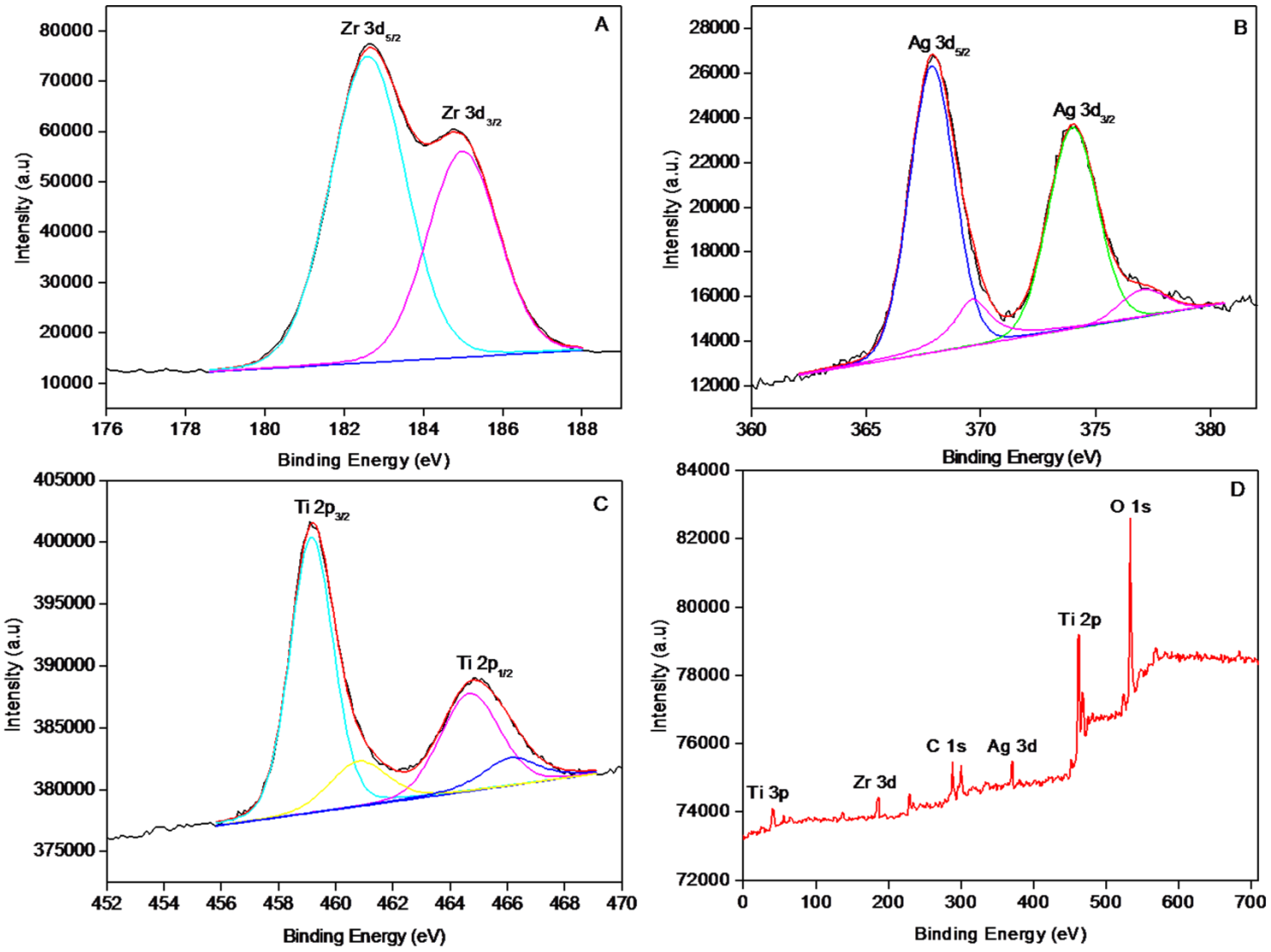
A
Zr 3d5/2
Zr 3d3/2
Intensity (a.u)
Binding Energy (eV)
B
Ag 3d5/2
Ag 3d3/2
Intensity (a.u.)
Binding Energy (eV)
C
Ti 2p3/2
Ti 2p1/2
Intensity (a.u)
Binding Energy (eV)
D
O 1s
Ti 2p
C 1s
Ag 3d
Zr 3d
Ti 3p
Intensity (a.u)
Binding Energy (eV)

Fig. 4

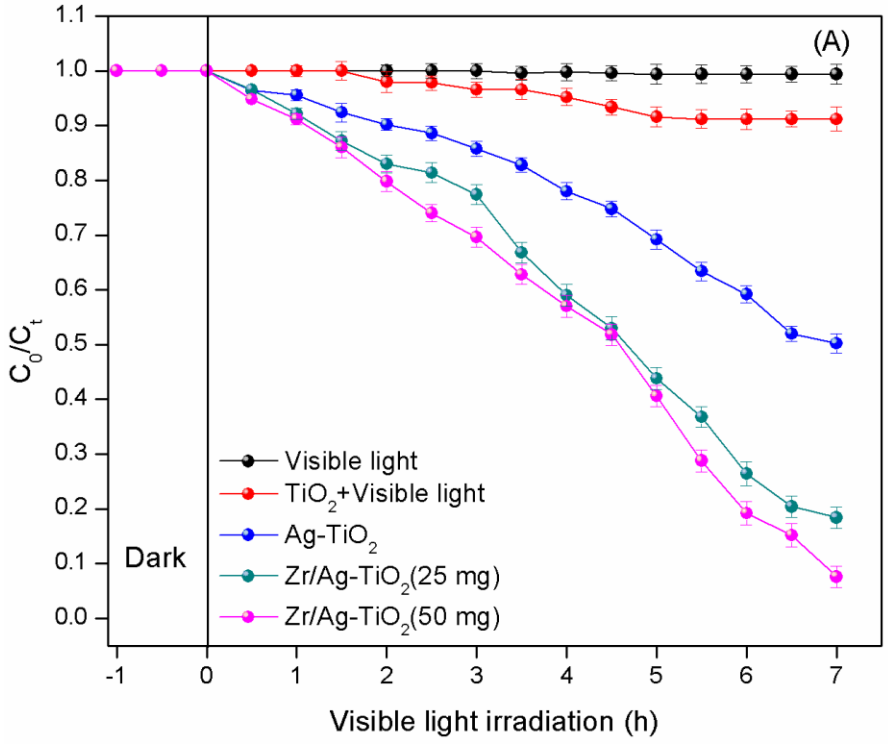
(A)
C_0/C_t
Dark
Visible light
TiO_2+Visible light
Ag-TiO_2
Zr/Ag-TiO_2(25 mg)
Zr/Ag-TiO_2(50 mg)
Visible light irradiation (h)

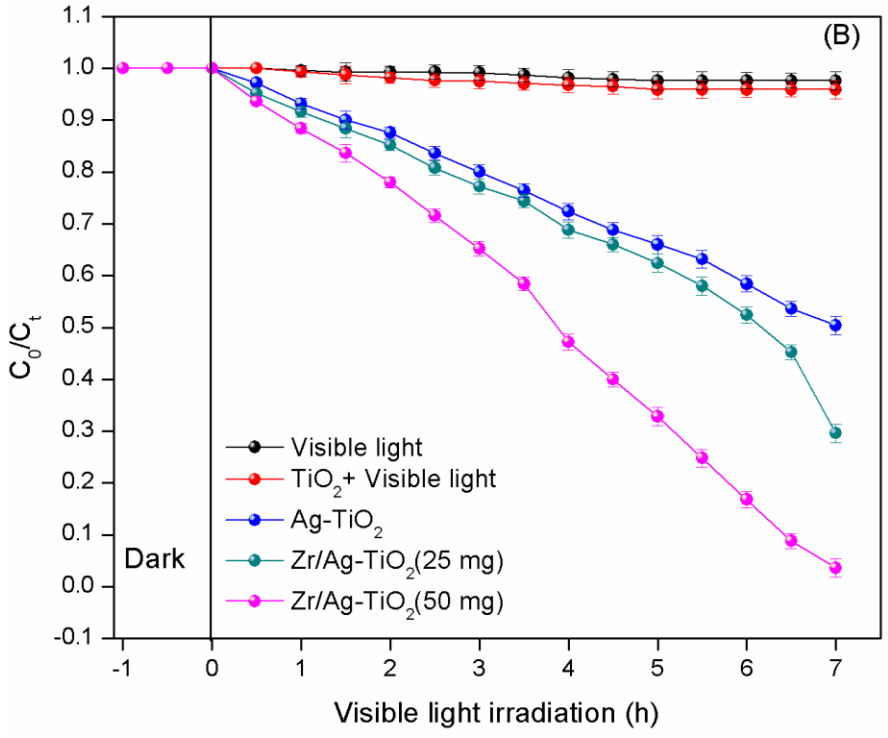
(B)
C_0/C_t
Dark
Visible light
TiO_2+ Visible light
Ag-TiO_2
Zr/Ag-TiO_2(25 mg)
Zr/Ag-TiO_2(50 mg)
Visible light irradiation (h)

Fig. 5

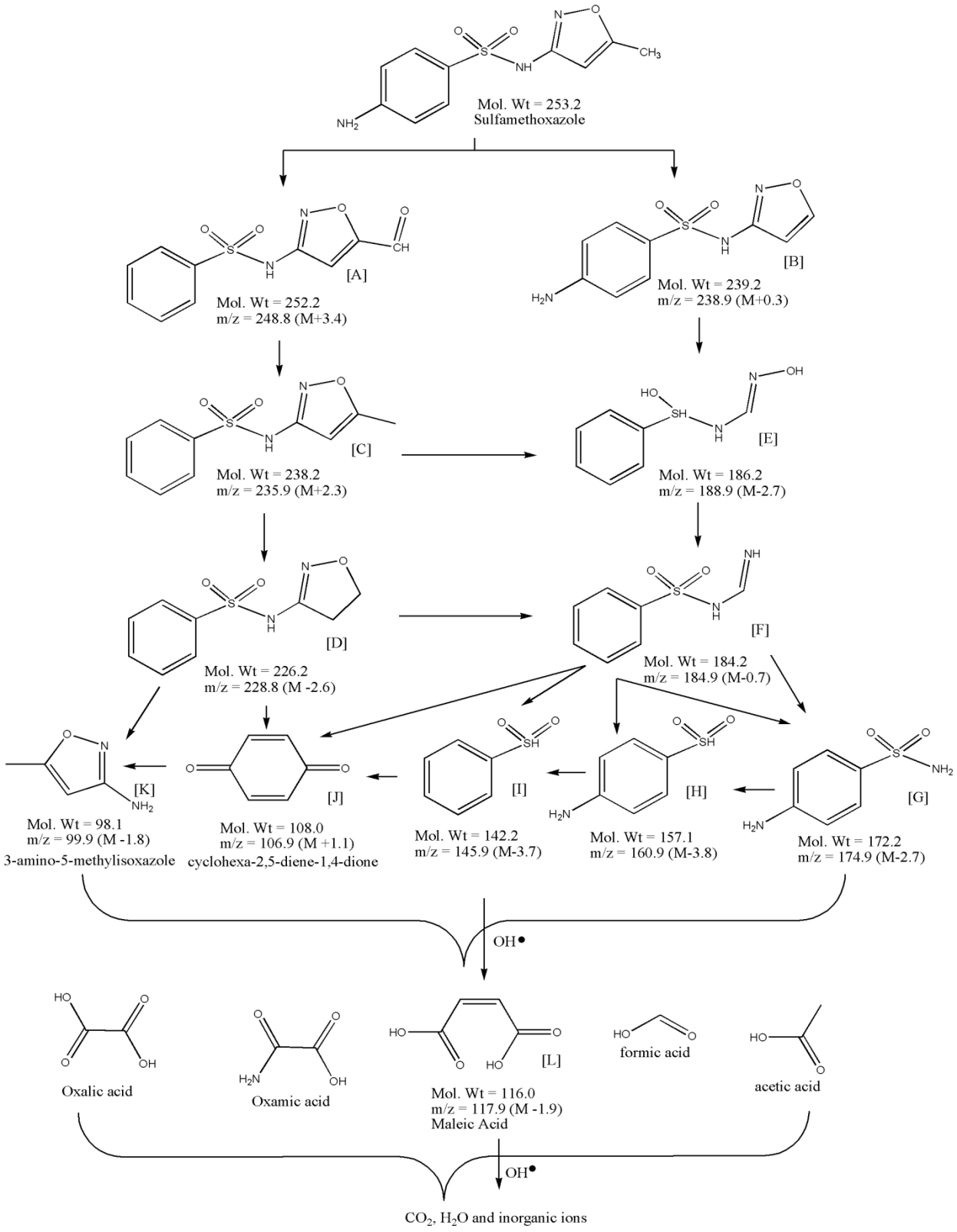
Mol. Wt = 253.2
Sulfamethoxazole
[A]
Mol. Wt = 252.2
m/z = 248.8 (M+3.4)
[B]
Mol. Wt = 239.2
m/z = 238.9 (M+0.3)
[C]
Mol. Wt = 238.2
m/z = 235.9 (M+2.3)
[E]
Mol. Wt = 186.2
m/z = 188.9 (M-2.7)
[D]
Mol. Wt = 226.2
m/z = 228.8 (M -2.6)
[F]
Mol. Wt = 184.2
m/z = 184.9 (M-0.7)
[K]
Mol. Wt = 98.1
m/z = 99.9 (M -1.8)
3-amino-5-methylisoxazole
[J]
Mol. Wt = 108.0
m/z = 106.9 (M +1.1)
cyclohexa-2,5-diene-1,4-dione
[I]
Mol. Wt = 142.2
m/z = 145.9 (M-3.7)
[H]
Mol. Wt = 157.1
m/z = 160.9 (M-3.8)
[G]
Mol. Wt = 172.2
m/z = 174.9 (M-2.7)
OH•
Oxalic acid
Oxamic acid
[L]
Mol. Wt = 116.0
m/z = 117.9 (M -1.9)
Maleic Acid
formic acid
acetic acid
OH•
CO2, H2O and inorganic ions

Fig.6

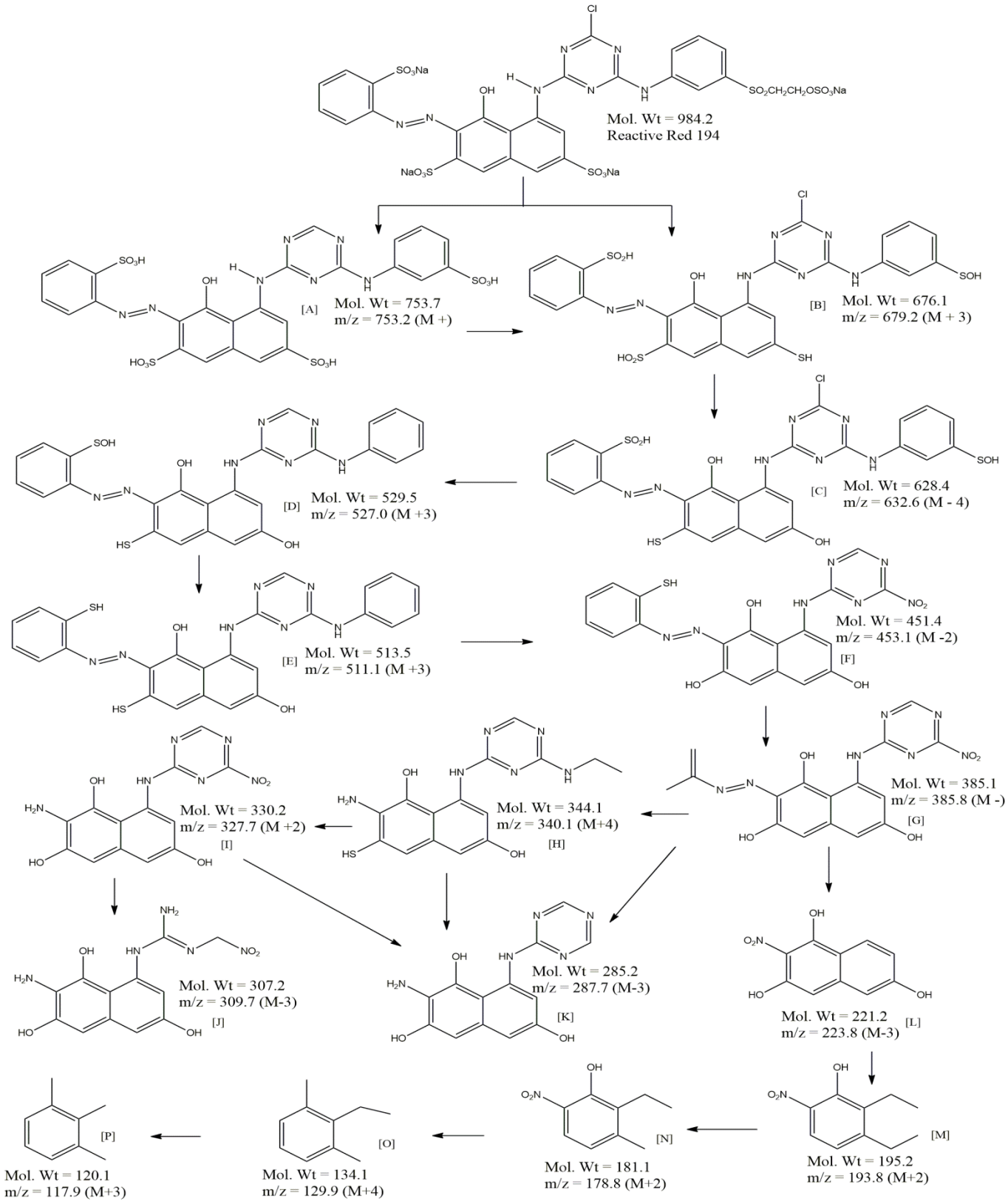
Mol. Wt = 984.2
Reactive Red 194
[A]
Mol. Wt = 753.7
m/z = 753.2 (M +)
[B]
Mol. Wt = 676.1
m/z = 679.2 (M + 3)
[C]
Mol. Wt = 628.4
m/z = 632.6 (M - 4)
[D]
Mol. Wt = 529.5
m/z = 527.0 (M +3)
[E]
Mol. Wt = 513.5
m/z = 511.1 (M +3)
[F]
Mol. Wt = 451.4
m/z = 453.1 (M -2)
[G]
Mol. Wt = 385.1
m/z = 385.8 (M -)
[H]
Mol. Wt = 344.1
m/z = 340.1 (M+4)
[I]
Mol. Wt = 330.2
m/z = 327.7 (M +2)
[J]
Mol. Wt = 307.2
m/z = 309.7 (M-3)
[K]
Mol. Wt = 285.2
m/z = 287.7 (M-3)
[L]
Mol. Wt = 221.2
m/z = 223.8 (M-3)
[M]
Mol. Wt = 195.2
m/z = 193.8 (M+2)
[N]
Mol. Wt = 181.1
m/z = 178.8 (M+2)
[O]
Mol. Wt = 134.1
m/z = 129.9 (M+4)
[P]
Mol. Wt = 120.1
m/z = 117.9 (M+3)

Fig.7

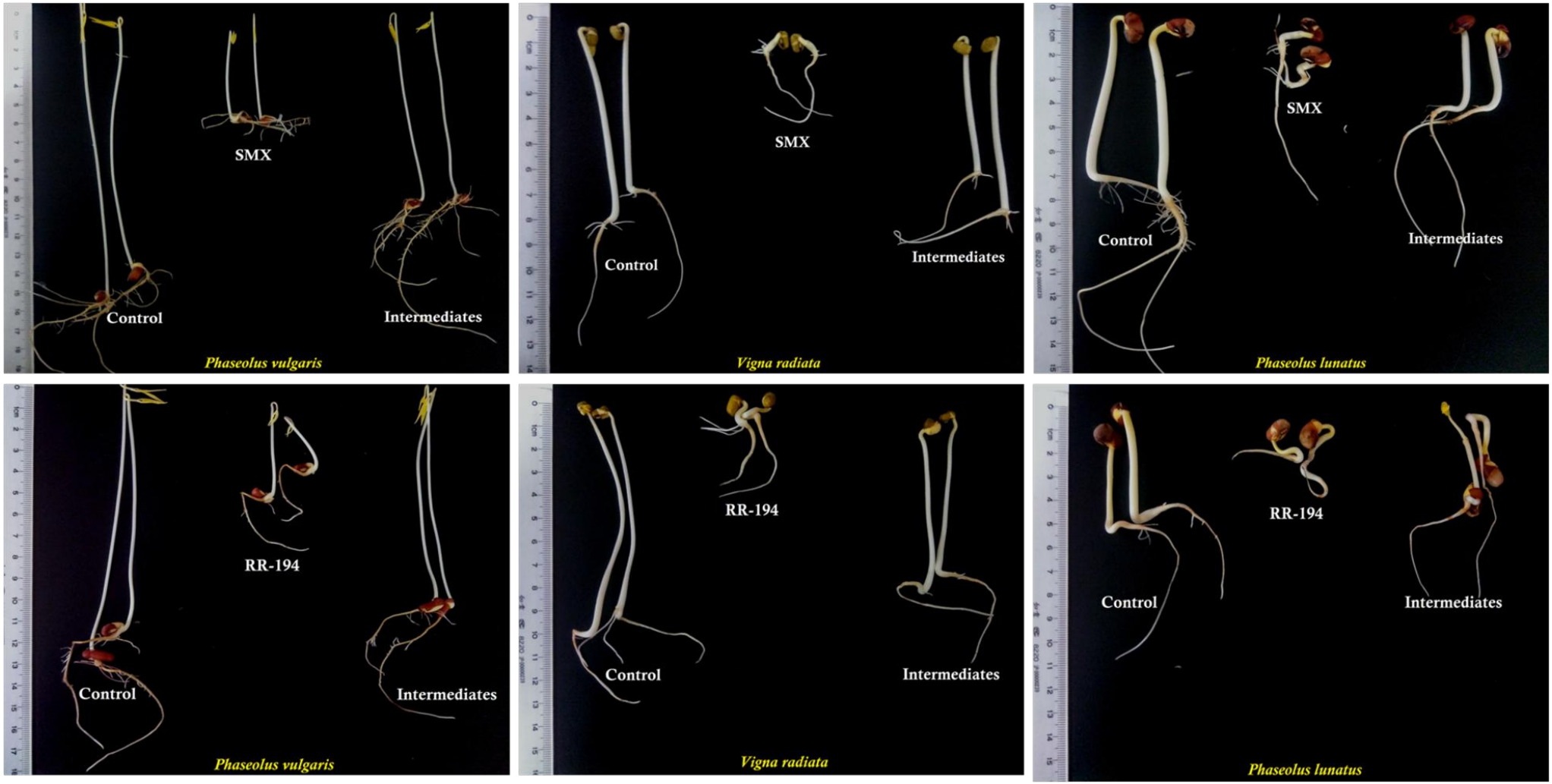
SMX
Control
Intermediates
Phaseolus vulgaris
SMX
Control
Intermediates
Vigna radiata
SMX
Control
Intermediates
Phaseolus lunatus
RR-194
Control
Intermediates
Phaseolus vulgaris
RR-194
Control
Intermediates
Vigna radiata
RR-194
Control
Intermediates
Phaseolus lunatus

Photocatalytic mineralization and degradation kinetics of sulphamethoxazole and reactive red 194 over silver-zirconium co-doped titanium dioxide: Reaction mechanisms, degradation products and phytotoxicity

Saraschandra Naraginti [a], Yi Li [a]*, Gianluca Li Puma [b]*

[a] Key Laboratory of Integrated Regulation and Resource Development on Shallow Lakes, Ministry of Education, College of Environment, Hohai University, Nanjing – 210098, PR China

[b] Environmental Nanocatalysis & Photoreaction Engineering, Department of Chemical Engineering, Loughborough University, Loughborough LE11 3TU, United Kingdom

Fig. S1 (a) UV–Vis spectra, (b) optical energy gap (Eg) and PL spectra (c) of the prepared nanoparticles

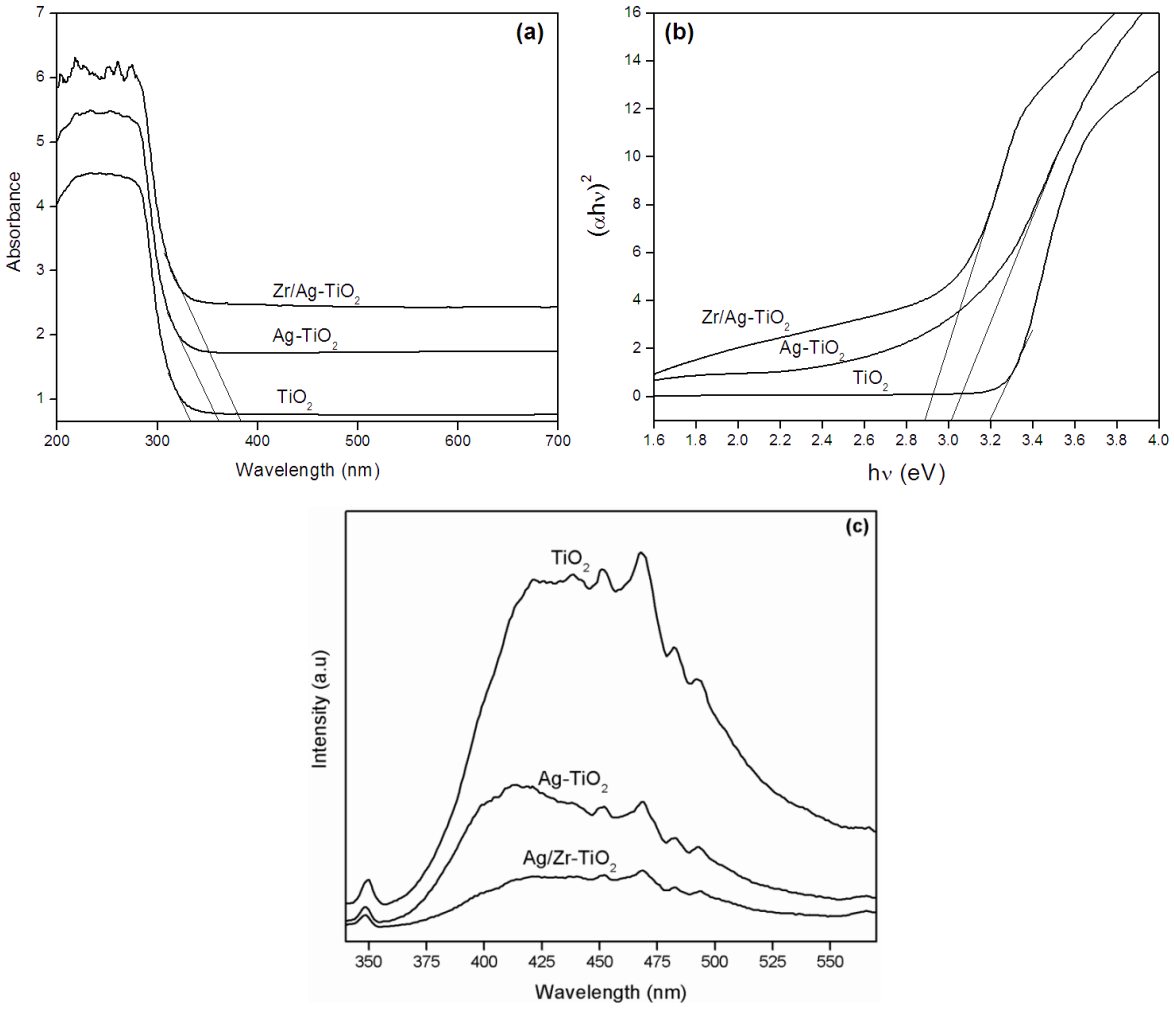

Fig. S2 TEM image of Ag-TiO_2 nanoparticles (a), HR-TEM image shows microstructure information (b), selected area electron diffraction pattern of the doped nanoparticles (c) and EDAX profile (d) showing the elements present in the doped nanoparticles

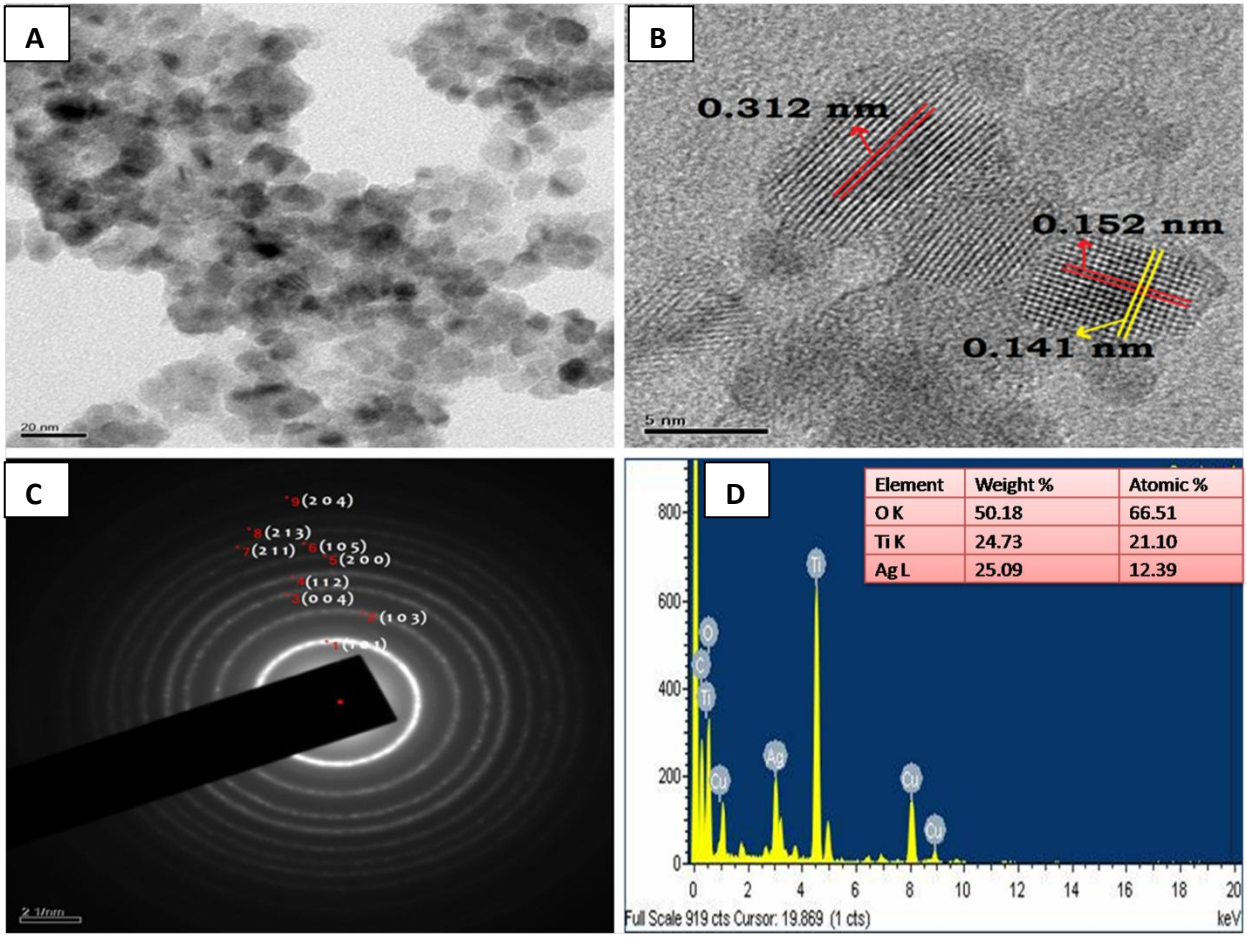

Fig. S3 TEM image of Zr/Ag-TiO_2 nanoparticles (a), HR-TEM image shows microstructure information (b), selected area electron diffraction pattern of the doped nanoparticles (c) and EDAX profile (d) showing the elements present in the doped nanoparticles

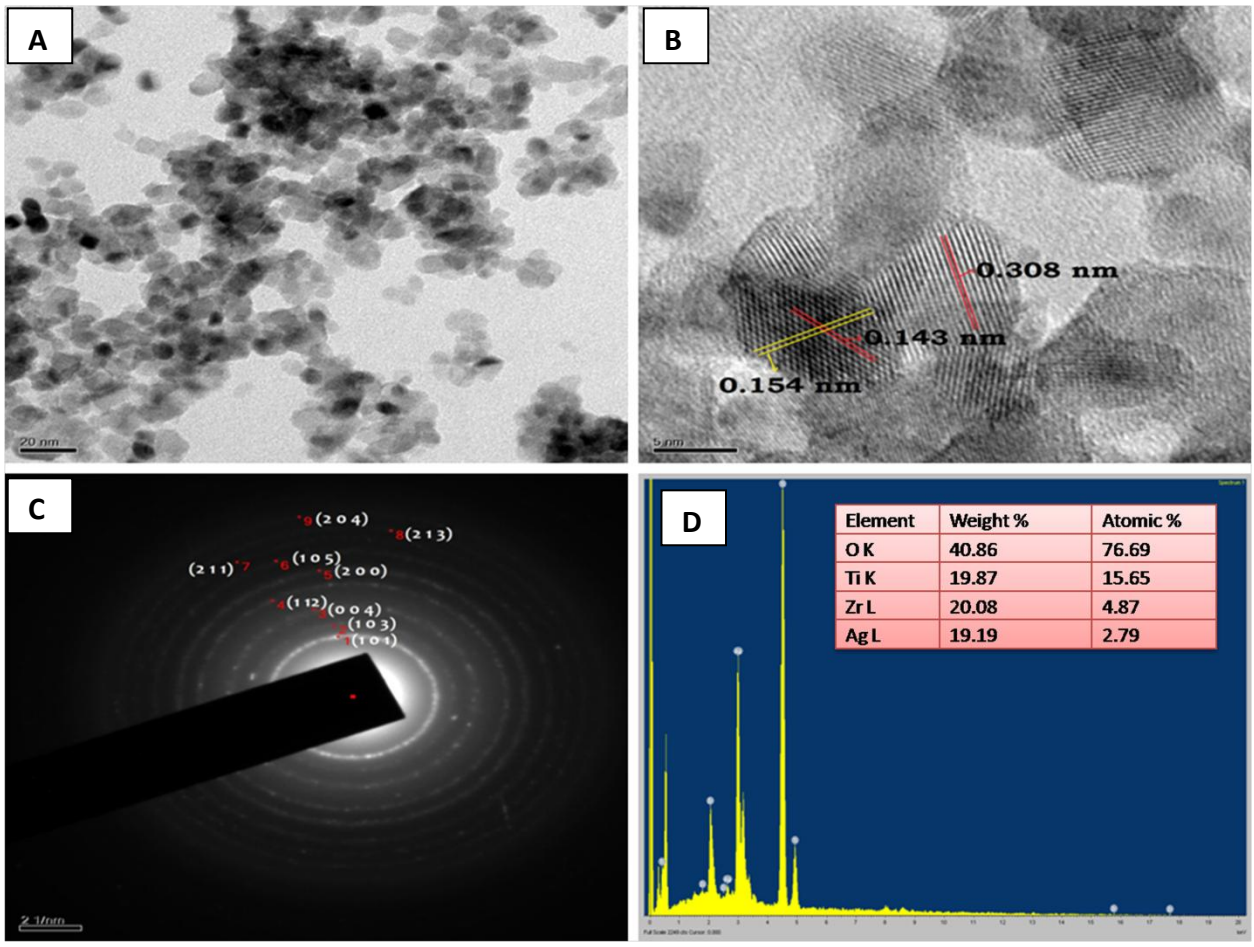

Fig. S4 LC/MS Chromatogram (a) of SMX degraded metabolites and LC/MS pattern (b, c & d)

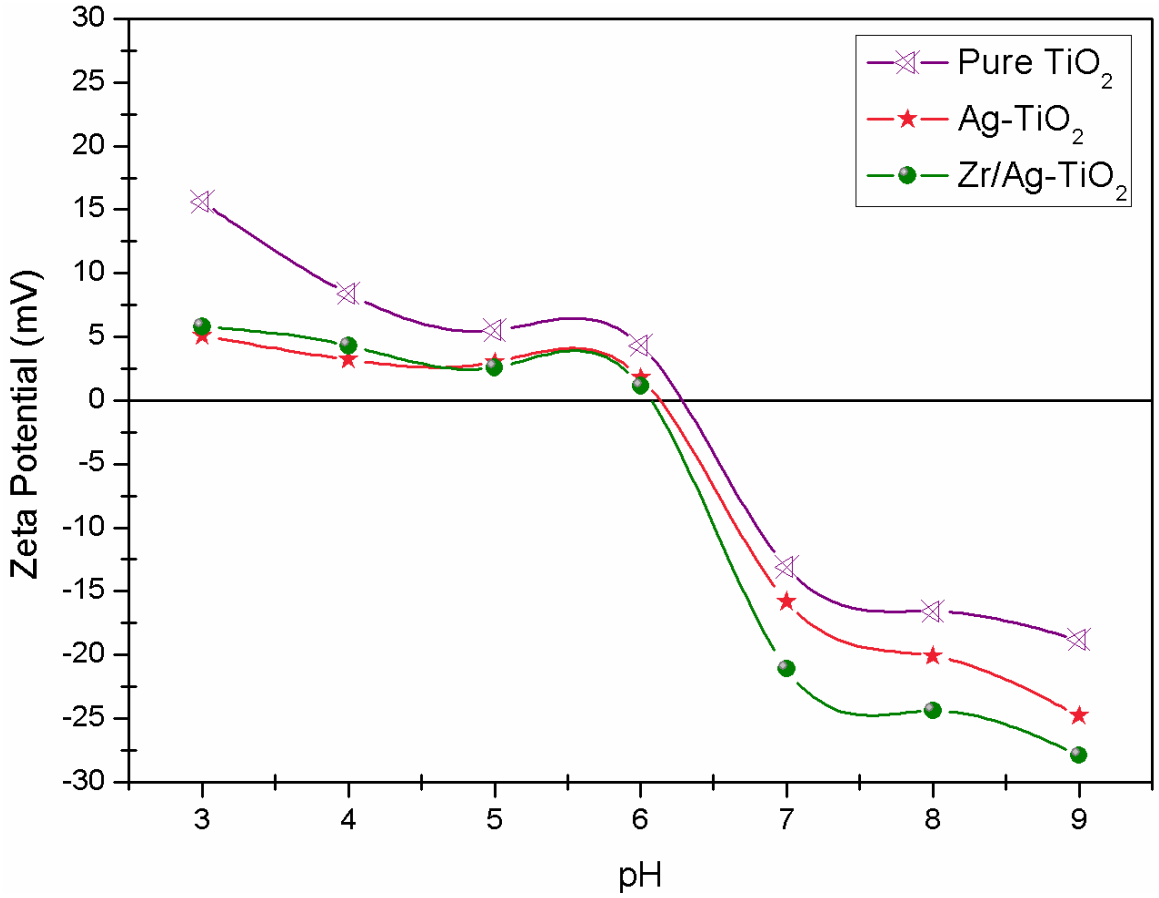

Fig. S5 LC/MS Chromatogram (a) of SMX degraded metabolites and LC/MS pattern (b, c & d).

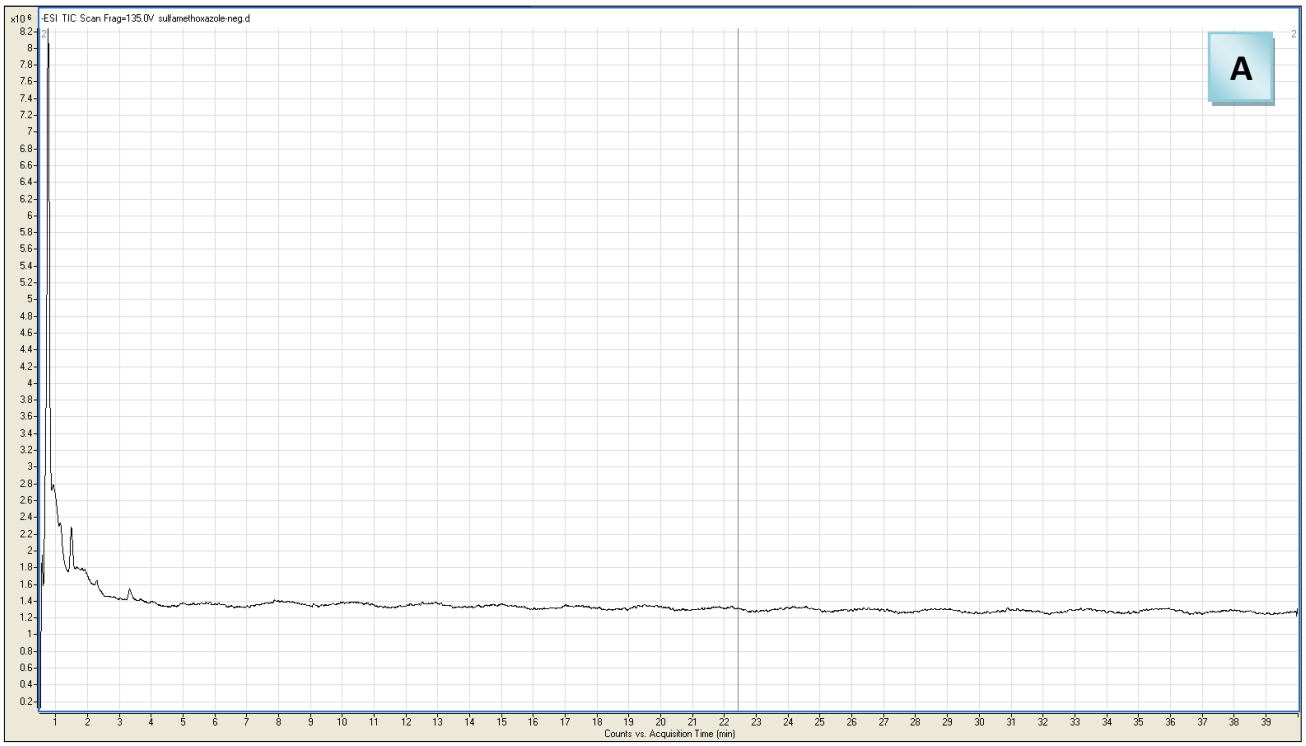

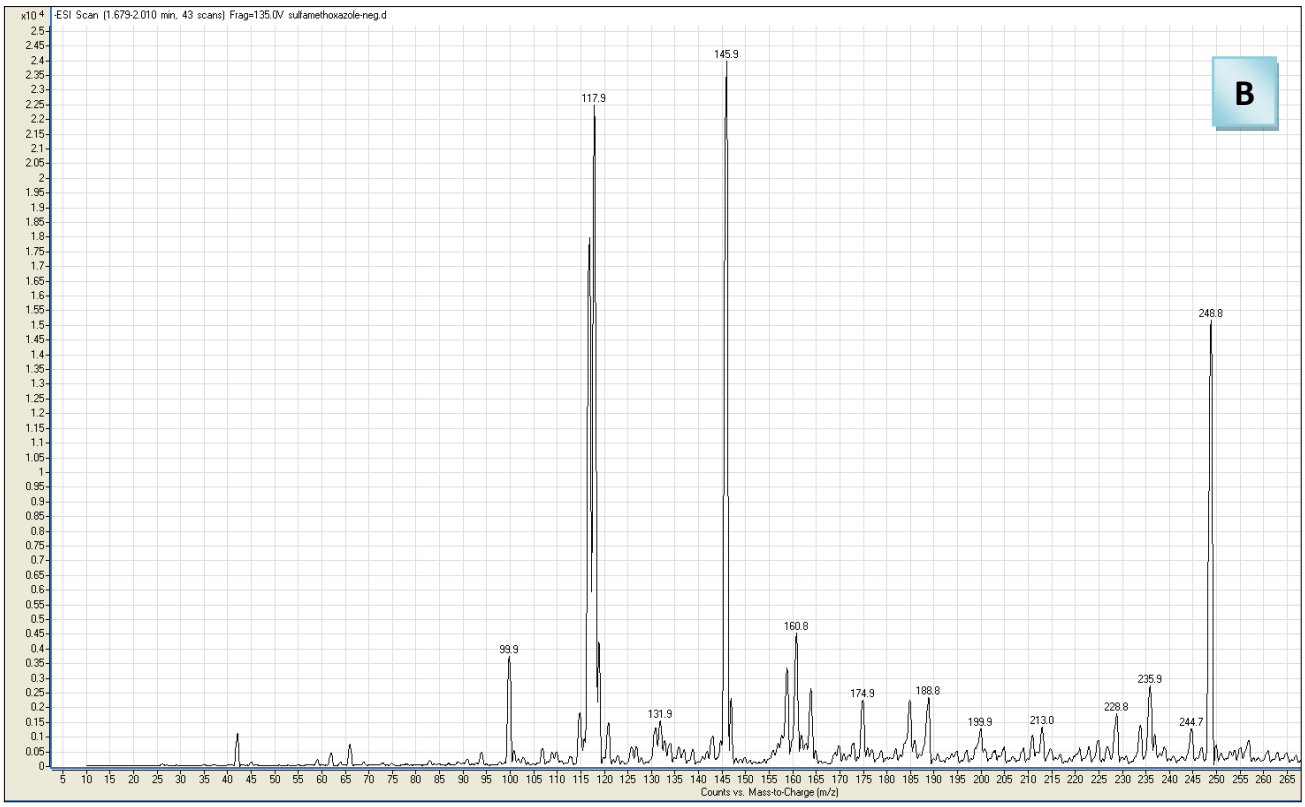

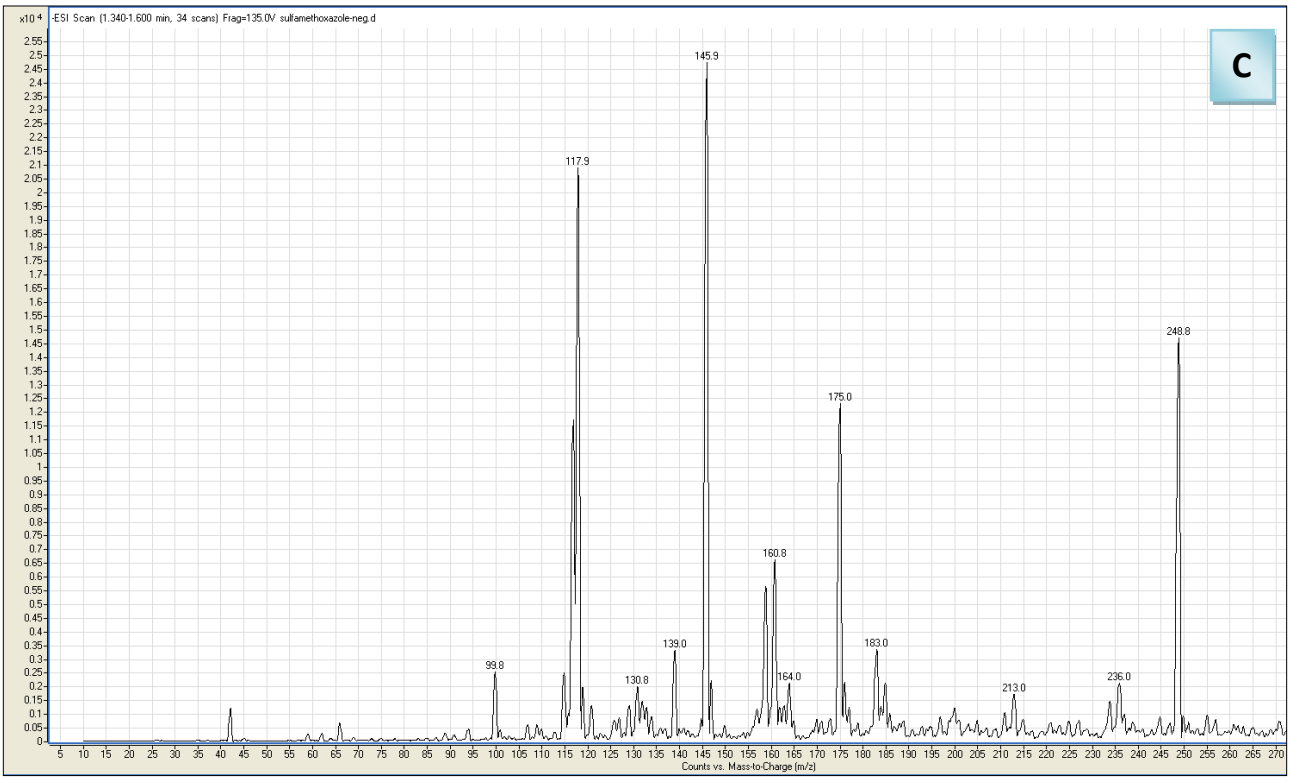
-ESI Scan (1.340-1.600 min, 34 scans) Frag=135.0V sulfamethoxazole-neg.d
x10 4
C
145.9
117.9
248.8
175.0
160.8
183.0
139.0
99.8
164.0
130.8
213.0
236.0
Counts vs. Mass-to-Charge (m/z)

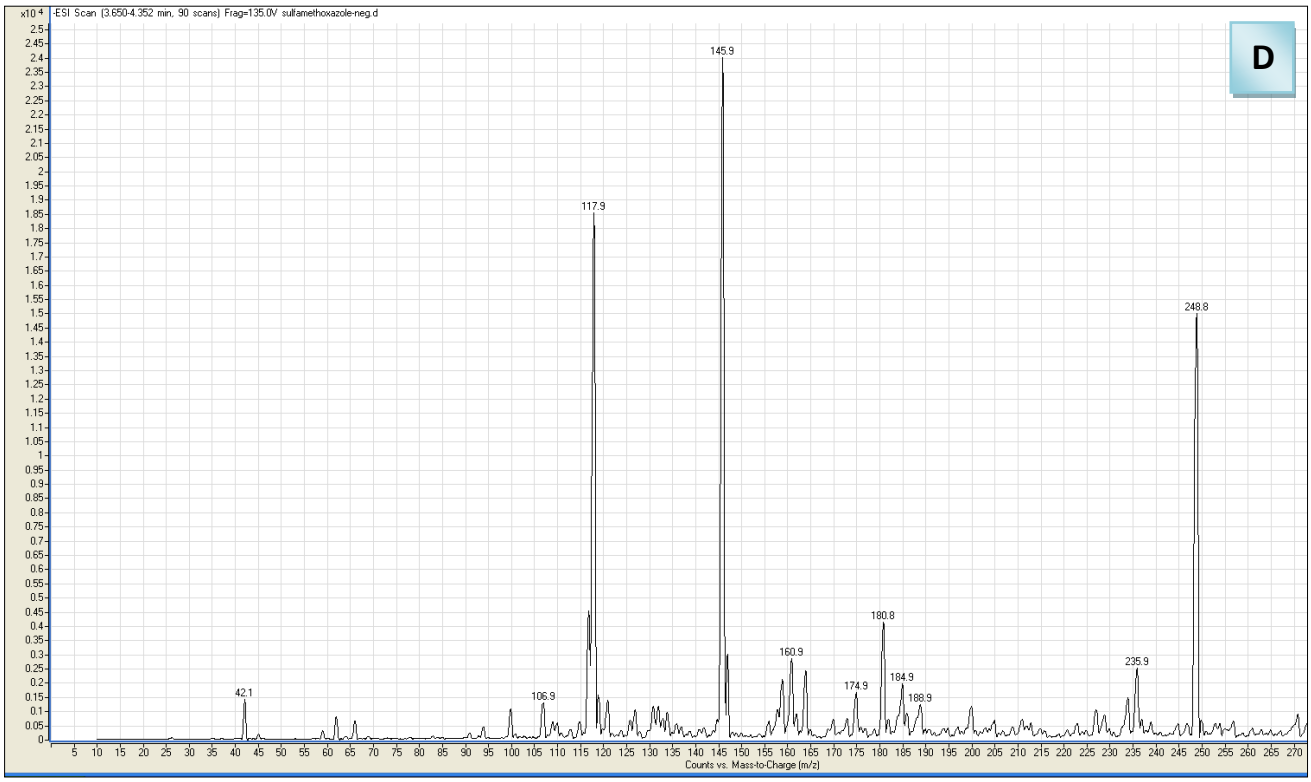
-ESI Scan (3.650-4.352 min, 90 scans) Frag=135.0V sulfamethoxazole-neg.d
x10 4
D
145.9
117.9
248.8
180.8
160.9
235.9
184.9
174.9
188.9
42.1
106.9
Counts vs. Mass-to-Charge (m/z)

Fig. S6 Fig. S4 LC/MS Chromatogram (a) of RR-194 degraded metabolites and LC/MS pattern (b, c & d).

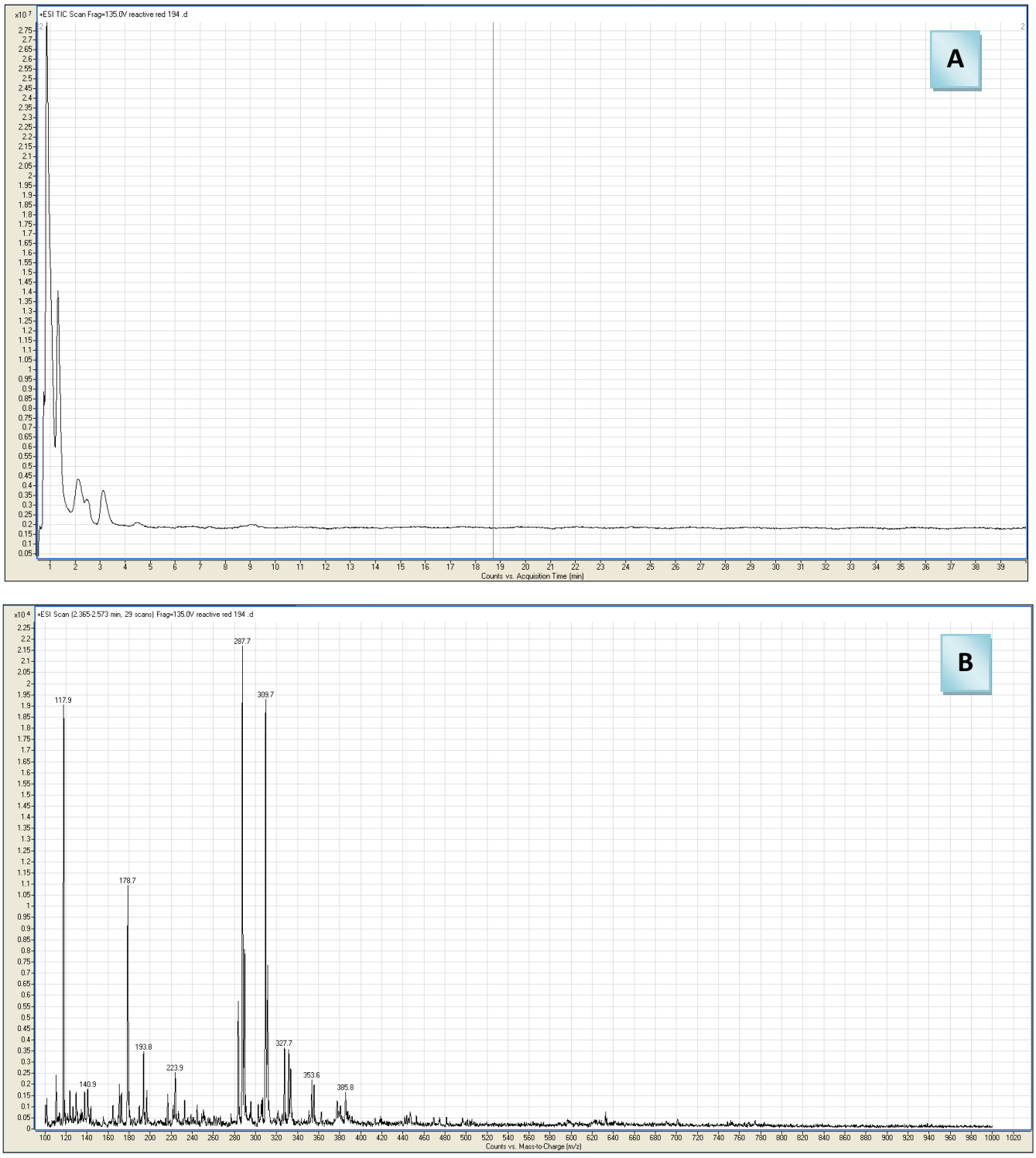

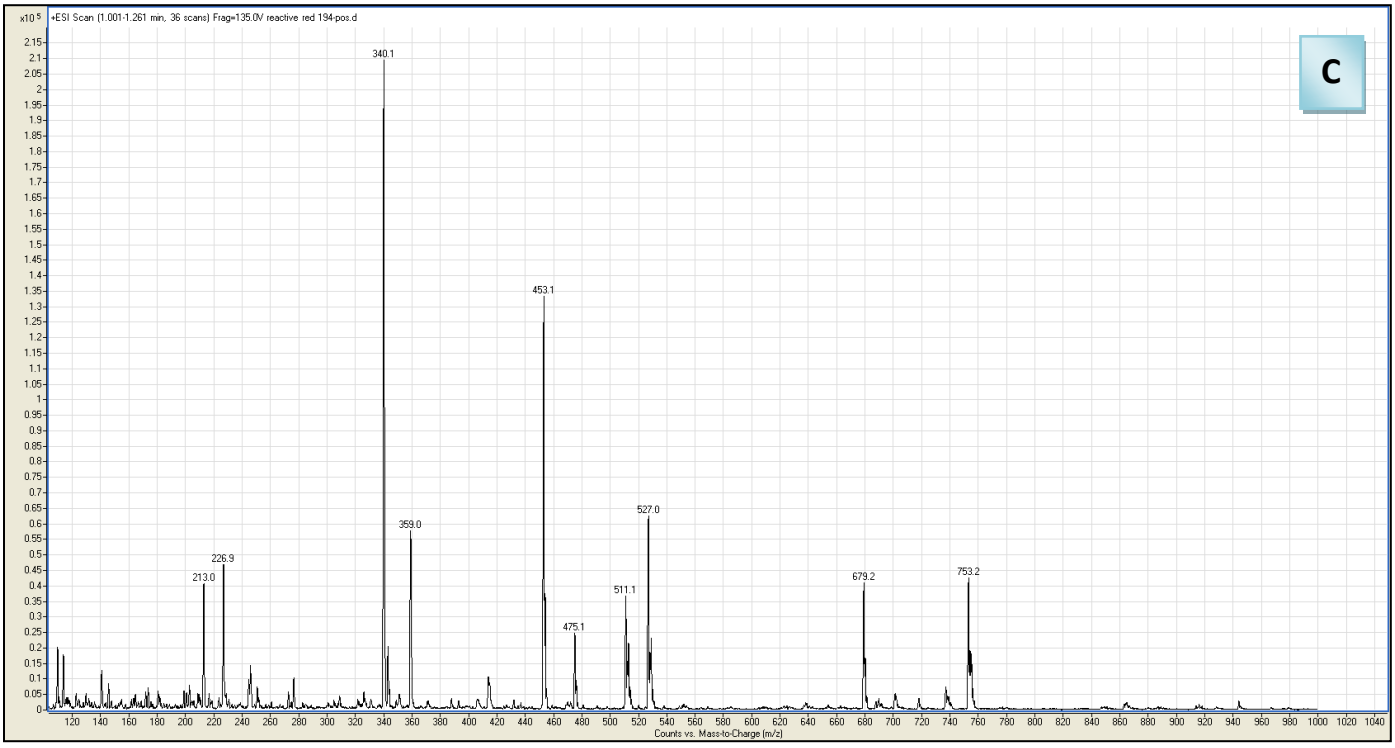
x10^5
+ESI Scan (1.001-1.261 min, 36 scans) Frag=135.0V reactive red 194-pos.d
C
340.1
453.1
359.0
527.0
226.9
213.0
511.1
679.2
753.2
475.1
Counts vs. Mass-to-Charge (m/z)

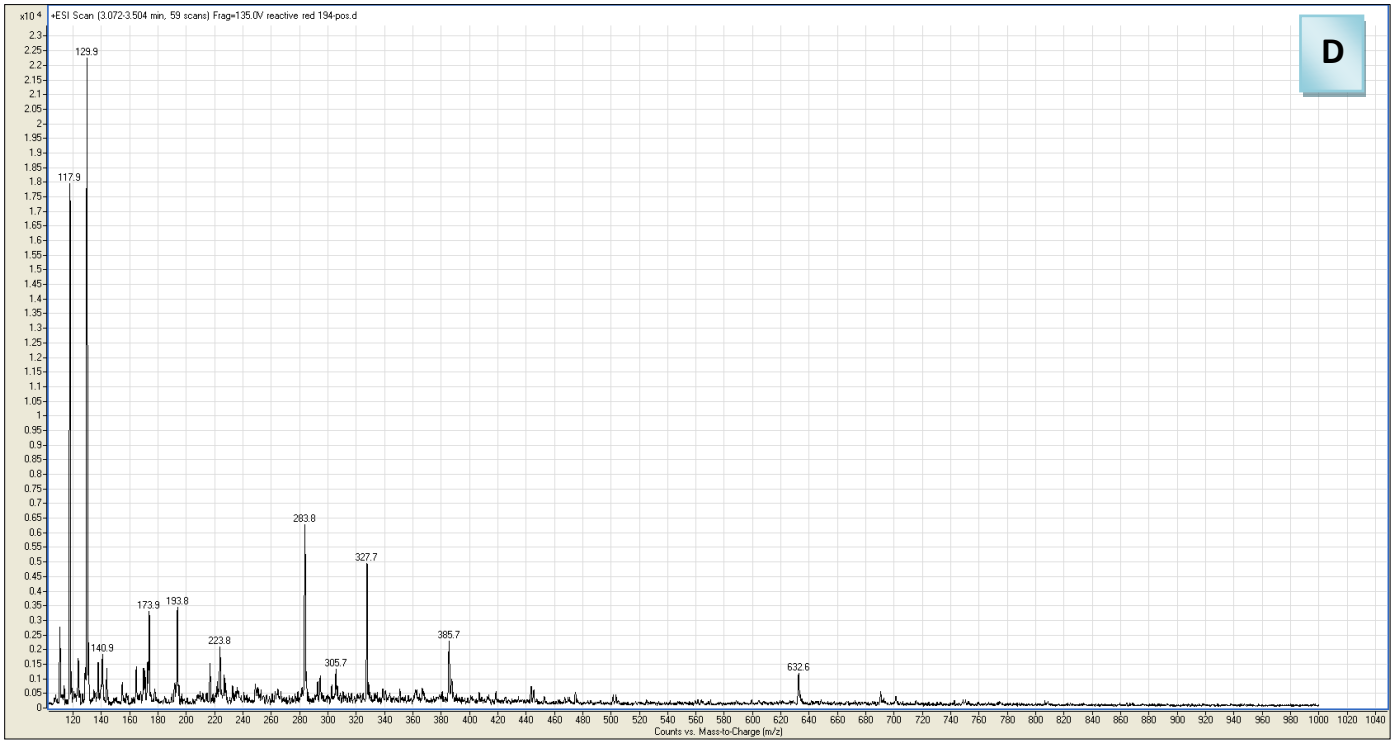
x10^4
+ESI Scan (3.072-3.504 min, 59 scans) Frag=135.0V reactive red 194-pos.d
D
129.9
117.9
283.8
327.7
173.9
193.8
223.8
385.7
140.9
305.7
632.6
Counts vs. Mass-to-Charge (m/z)

Fig.S7 Active species scavenging experiments using Zr/Ag-TiO_2 during SMX (a) and RR-194 (b) degradation

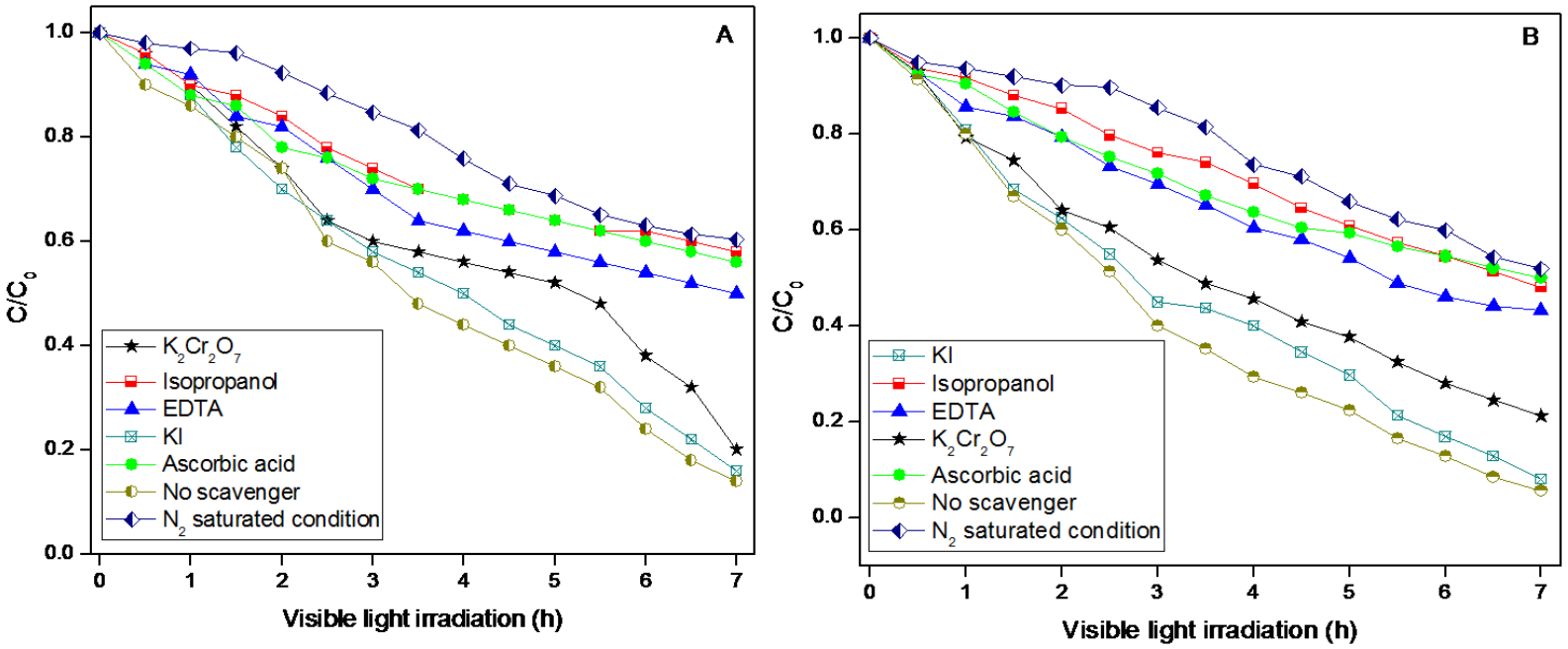

Fig.S8 Concentration of •OH (a) and •O_2− (b) radicals at different time intervals

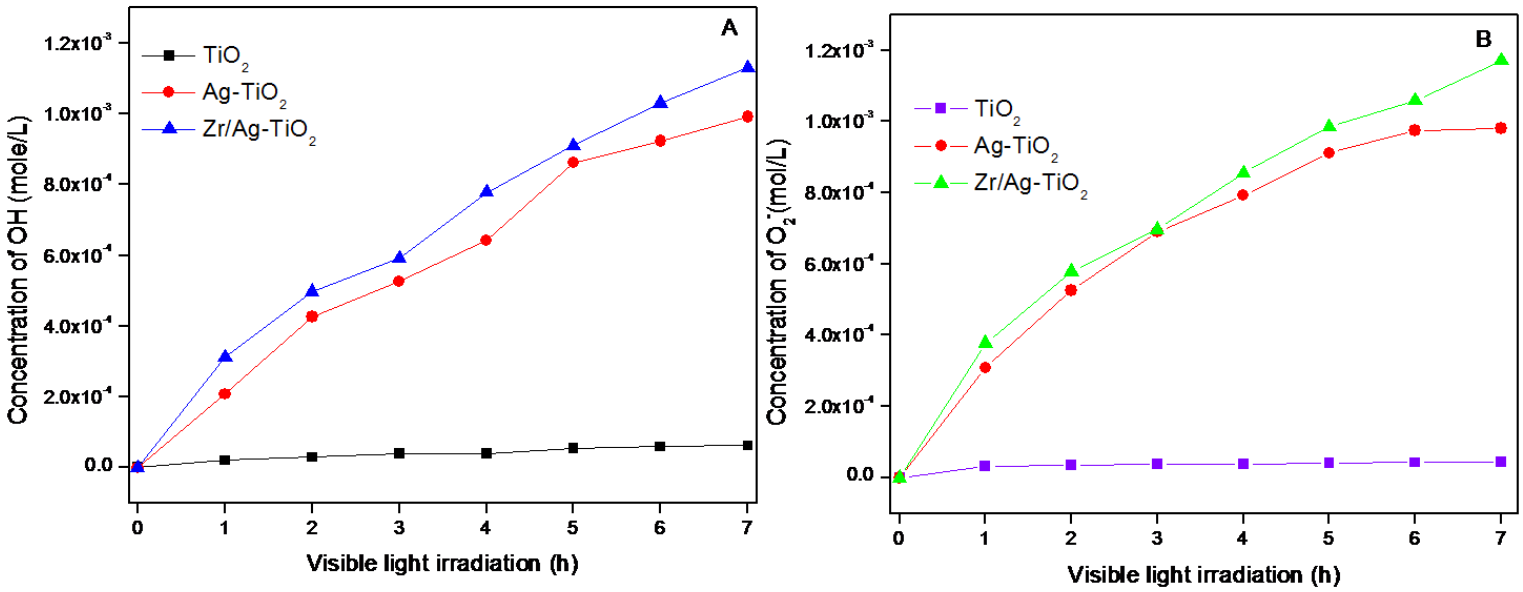

Scheme 1. Reaction pathway between NBT and superoxide radicals with the formation of formazan

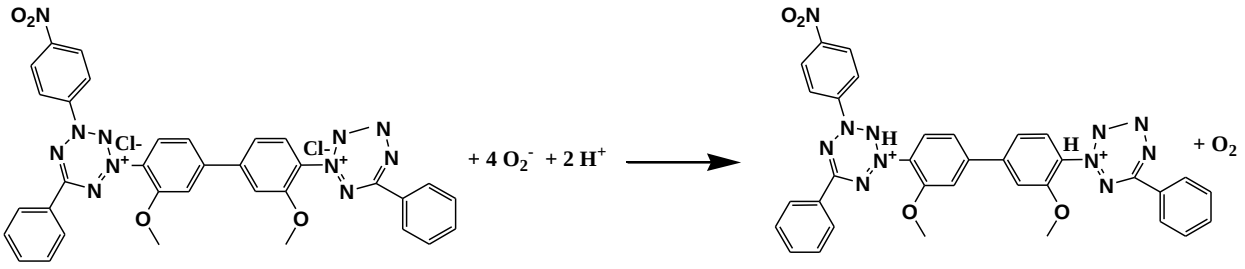

Nitroblue tetrazolium chloride **Formazan**

Scheme 2. Reaction pathway between terepthalic acid and hydroxyl radical with the formation of fluorescent 2-hydroxy terepthalic acid

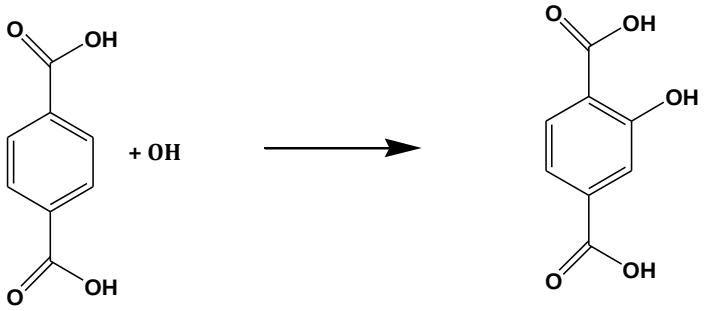

Terepthalic acid (non-flourescent) **2-hydroxy terepthalic acid (flourescent)**